Lithium-Sulfur Batteries: Investigation of Sulfur Loading and Carbon Templating

---

A Thesis
Presented to
the faculty of the School of Engineering and Applied Science
University of Virginia

---

in partial fulfillment
of the requirements for the degree
Master of Science

By

Charles Michaelis

May 2017

Table of Contents

Figures 3
Tables 4
Abbreviations 4
1. Abstract 5
2. Background 5
  2.1 Li-ion Electrode Technology 5
  2.2 Lithium-Sulfur Battery Chemistry 8
  2.3 Polysulfide Shuttling and Sulfur Migration 10
  2.4 Carbon Material Development 12
3. Sulfur Sublimation 15
  3.1 Introduction 15
  3.2 Materials and Methods 15
    3.2.1 Electrode Fabrication and Sulfur Sublimation 15
    3.2.2 Cycling 16
  3.3 Results and Discussion 17
  3.4 Conclusion 21
4. Sulfur Loading 22
  4.1 Introduction 22
  4.2 Materials and Methods 23
    4.2.1 Electrode and Cell Fabrication 23
    4.2.2 Coin Cell Testing 23
    4.2.3 Materials Characterization 24
  4.3 Results and Discussion 24
  4.4 Conclusions 30
5. Polystyrene Particle Synthesis 31
  5.1 Introduction 31
  5.2 Materials and Methods 32
  5.3 Results and Discussion – Particle Synthesis 32
  5.4 Conclusion 35
6. Inverse Opal and Pluronic Templated Carbon Materials 36
  6.1 Introduction 36

6.2 Materials and Methods 37
6.2.1 Colloidal Opal Assembly 37
6.2.2 Inverse Opal Carbon Fabrication 38
6.2.3 Electrode and Cell Fabrication 38
6.2.4 Pluronic Templated Carbon Fabrication 39
6.2.5 Analytical Testing – Raman, Surface Area and Pore Analysis, SEM 39
6.3 Results and Discussion 40
6.3.1 Inverse Opal Carbon 40
6.3.2 Pluronic Templated Carbon 45
6.4 Conclusion 48
7. Final Conclusions 48
8. Acknowledgements 49
Works Cited 50

Figures

Figure 1: Layered graphite with lithium ion (black circle) being inserted into the structure. The graphite is reduced via electrons from the current collector, localizing to the six carbon rings in the graphite structure. 6
Figure 2: Example sequence of reactions during discharge of Li-S electrochemical cell. PS species (Li_2S_n) can have a variety of n values. All reactions for soluble species ($n > 2$) occur during PS adsorption on the electrode surface, while insoluble species ($n < 2$) remain on the surface after reaction. 10
Figure 3: Example PS shuttling reactions, where long PS chains are reduced at the anode and shorter chains oxidized at the cathode, resulting in internal energy release during charging. 11
Figure 4: Scanning electron micrograph of inverse opal carbon. Scale bar 1 µm. 14
Figure 5: Sulfur mass as a function of time undergoing treatment in vacuum oven for electrodes that initially contain 18 (blue circles) and 36 (orange circles) weight percent sulfur. 17
Figure 6: Cycling performance of Li-S battery electrode that underwent vacuum drying before cycling. 36 wt% sulfur cathode, cycle rate 0.05 C. 18
Figure 7: Coulombic efficiency of sample prepared at 18 wt% S (orange circles) and sample that underwent sulfur sublimation treatment with a final 20 wt% S (blue triangles). 20
Figure 8: Discharge capacity of sample prepared at 18 wt% S (orange circles) and sample that underwent sulfur sublimation treatment with a final 20 wt% S (blue triangles). 20
Figure 9: Charge/discharge profiles at different sulfur loadings at a rate of 0.1 C. 25
Figure 10: SEM (top row) and EDS of carbon (middle) and sulfur (bottom) of carbon-sulfur electrodes. (Scale bar: 400 µm) 26

Figure 11: Average gravimetric discharge capacity as a function of C rate and sulfur content. Error bars represent the standard deviation of a minimum of 4 electrodes and 20 cycles were used for each C rate and electrode loading. 28
Figure 12: Initial gravimetric capacity vs. average sulfur thickness for our results (orange squares) and a variety of literature sources[34–42] 29
Figure 13: Estimated voltage drop (V) due to electron conductivity through the sulfur layer vs. S thickness (nm) at different C rates 30
Figure 14: The average particle diameters plotted against the initial styrene content (blue circles) and simple model relating initial mass and particle diameter governed by Eq. 7. 35
Figure 15: IOC-390 BJH data, Pore volume (blue circles) and dV(r) (orange). 41
Figure 16: Rate capability comparison between Carbon Black and Inverse Opal electrode performances. Electrodes were cycled 5 times at each C rate: 0.1, 0.2, 0.5, 1, and 2 C 42
Figure 17: IOC-270 (top) and IOC-390 (Bottom). Scale bars 5 µm. 43
Figure 18: Raman spectrograph of 370 nm IOC. 44
Figure 19: BJH pore volume and dV(r) of PLC. 45
Figure 20: Raman spectrograph of PLC electrode impregnated with sulfur. 46
Figure 21: Voltage profiles (36 wt% S) PLC (orange) and carbon black (blue) Li-S cells. 47

Tables

Table 1: Yield and PDI for seven batches of spherical polystyrene particles. 33

Abbreviations

Li-ion	Lithium-ion
Li-S	Lithium-Sulfur
SC	Sulfur Carbon
PS	Polysulfide
IOC	Inverse Opal Carbon
PLC	Pluronic Carbon
DLS	Dynamic Light Scattering

1. Abstract

While showing promise as an alternative to lithium-ion (Li-ion) rechargeable batteries, lithium-sulfur (Li-S) batteries still face several hurdles before becoming competitive with current commercial batteries. In this work, we explore several avenues for improvement and overall understanding of the Li-S system. A thorough study of the effects of sulfur content on Li-S cell, including controlled sublimation of sulfur to moderate loading, showed several factors that contribute to sulfur performance. Preliminary study was conducted towards syntheses of hierarchical carbon support with the goal of mitigating polysulfide shuttling and maximizing the full energy storage potential of Li-S batteries by combining meso- and microporous structures within the carbon matrix.

2. Background

2.1 Li-ion Electrode Technology

Li-ion batteries are commonplace in our lives today, powering phones, computers, power tools, and cars. Most conventional Li-ion batteries implement intercalation chemistry materials for both electrodes[1]. In intercalation chemistry, lithium ions are added into and removed from crystalline metal oxides and graphitic carbons host interstitial sites (e.g. $LiCoO_2$, $LiMn_2O_4$, etc.)[1]. This process is highly reversible, providing reliable electrodes for mass production.

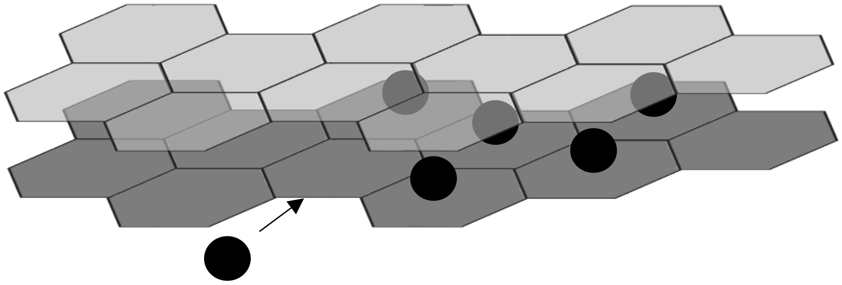

Figure 1: Layered graphite with lithium ion (black circle) being inserted into the structure. The graphite is reduced via electrons from the current collector, localizing to the six carbon rings in the graphite structure.

A graphite/lithium cobalt oxide cell is the most common Li-ion electrode chemistry. During the charge process, graphite, the anode, accepts the lithium ion and an electron in a reduction reaction (Figure 1, Eq. 1). Simultaneously at the cathode, lithium cobalt oxide is oxidized and releases a lithium ion from its solid lattice into the electrolyte (Eq. 2). The battery takes advantage of the electrochemistry of the system by separating the reduction and oxidation processes, storing electrical energy on charge, and releasing electrical energy on discharge. During charging, energy is added to the battery by applying an external electrical potential, driving electrons from the cathode to the anode. To maintain charge neutrality, positively charged lithium ions diffuse through the electrolyte from the cathode to the anode. The specific reactions (the forward reactions correspond to charge, reverse reactions correspond to discharge) for the graphite/lithium cobalt oxide system are as follows:

$$C_6 + Li^+ + e^- \rightleftharpoons LiC_6 \tag{1}$$

$$LiCoO_2 \rightleftharpoons x\,Li^+ + xe^- + Li_{1-x}CoO_2, \tag{2}$$

A common electrolyte is lithium hexafluorophosphate in an ethylene carbonate and dimethyl carbonate mixture (EC-DMC/$LiPF_6$)[2].

Several drawbacks arise when implementing these anode and cathode materials. The fragility of graphite when used as the anode in Li-ion batteries is the biggest concern; graphite is susceptible to both cracking and exfoliation during normal and extreme battery conditions[3]. Cracking can result from external stress, as well as from the production of ionic and gaseous compounds in the electrode during cycling[3]. Exfoliation can occur due to larger ions being inserted into the graphite, and causes cracking in graphite under more extreme polarization environments[3]. Lithium cobalt oxide is expensive due to the scarcity of cobalt metal[4], and makes the final battery relatively heavy due to its low specific energy[5], especially for large scale applications like cars. Successive cycling of the lithium cobalt oxide material can lead to cracking and overall loss in structural integrity of the electrode, decreasing performance and longevity[4]. For many common Li-ion materials, lithium insertion is limited to one lithium ion per transition metal atom and no reaction with other structural atoms, limiting overall capacity[6]. Some modifications can be made to the structure of crystalline metal oxides to increase the lithium insertion ratio, but are generally unstable in Li-ion battery applications[6]. Finally, decomposition of the electrolyte, resulting in gas evolution or even combustion, is a major concern[6]. Because carbon is used as the anode material, the operational voltage of the battery is outside the stability window of the electrolyte[6], leading to degradation of the electrolyte and evolution of flammable gasses. Although different techniques have been used to mitigate electrolyte decomposition, it still deserves consideration when comparing the advantages and disadvantages of different battery chemistries.

Lithium metal anodes, which are used commonly in experimental research batteries[7], offer several benefits relative to common Li-ion battery anodes such as graphite. Metallic lithium has a very high theoretical capacity (3860 mAh/g), maximizing energy storage density[8]. Metallic lithium's low electrochemical potential (-3.045 V vs SHE), maximizes the voltage difference between the cathode and anode, resulting in high power output and energy storage. Finally, lithium's low atomic mass makes it well suited for minimizing battery weight in any application. Unfortunately, lithium metal anodes suffer from several problems that have prohibited their use in industrial and commercial applications, including dendrite growth and poor coulombic efficiency[6]. Dendritic growth is the formation of thin columns of lithium metal on the surface of the anode instead of evenly spread deposition of lithium ions during cycling[8]. These growths cause an increase in the volume of the lithium electrode over time, and in more extreme cases the more serious problem of short circuiting the battery internally, resulting in a fire[6]. These factors make lithium anodes unfit for commercial use, but small scale use in laboratories is safe and effective.

2.2 Lithium-Sulfur Battery Chemistry

Considerable research has been conducted to increase performance, decrease cost, and limit the environmental and health impacts of consumer batteries. Lithium-sulfur (Li-S) batteries show promise in addressing some of these challenges. The major components in Li-S batteries are lithium, carbon, sulfur, and electrolyte. Sulfur and carbon are widely available, making them inexpensive and ideal for mass production. When compared with other Li-ion technologies, e.g. lithium metal oxide materials, Li-S has several advantages. Li-S has a theoretical energy storage density of 2600 Wh/kg[9], compared with 150 Wh/kg practical[5] (out of 986 Wh/kg theoretical[10]) for commercial Li-ion batteries. A final Li-S battery would be lower in overall mass, and would contain carbon and sulfur as opposed to heavy metal oxides. Even accounting for differences in capacity and power output, Li-S would be cheaper to manufacture when optimized, specifically comparing sulfur costs to metal oxide materials[11].

It is important to understand the unique electrochemical reactions of Li-S batteries in order to implement directed steps toward improving the technology. During a typical discharge, a series of chemical steps proceed at the cathode to release energy from the elemental sulfur. As opposed to intercalation chemistry of metal oxides, Li-S redox reactions undergo conversion chemistry[12]. Conversion chemistry in Li-S batteries converts individual S_8 molecules to Li_2S, operating on a per-molecule basis as opposed to inserting lithium into a larger crystal structure. The series of reactions follows:

$$S_8 + 2Li^+ + 2e^- \rightarrow Li_2S_8 \qquad (3)$$

$$Li_2S_8 + 2Li^+ + 2e^- \rightarrow Li_2S_{8-n} + Li_2S_n \qquad (4)$$

$$2Li_2S_n + (2n-4)Li^+ + (2n-4)e^- \rightarrow nLi_2S_2 \qquad (5)$$

$$Li_2S_n + (2n-2)Li^+ + (2n-2)e^- \rightarrow nLi_2S \qquad (6)$$

$$Li_2S_2 + 2Li^+ + 2e^- \rightarrow 2Li_2S \qquad (7)$$

Elemental sulfur, S_8, accepts two electrons from the external circuit and two lithium ions from the electrolyte, producing a polysulfide (PS) with composition Li_2S_8 (Equation 3, Figure 2a). This long PS chain is soluble in the electrolyte[9]. The solubility of electrode material in the electrolyte is uncommon in Li-ion batteries, and introduces several problems specific to the Li-S system. These issues, specifically sulfur loss and PS shuttling, will be discussed in detail in the next section. Next, the sulfur in long PS chains undergoes further reduction, splitting into shorter chains such as Li_2S_4 (Equation 4, Figure 2b). These species are also soluble in the electrolyte[9]. In the third step, short PS species are converted to insoluble lithium disulfide and lithium sulfide (Equations 5 and 6, Figure 2c,2d) Li_2S_2 and Li_2S are deposited on the surface of the carbon substrate. Finally, lithium disulfide species are reduced to lithium sulfide (Equation 7), and the discharge process is complete. It is important to note throughout all of these reactions, anodic lithium is being oxidized from Li to Li^+, and the resulting electron transferred through the external circuit (Figure 2). The presented reactions take place in reverse order during a charge cycle, lithium sulfide chains growing until returning to elemental sulfur.

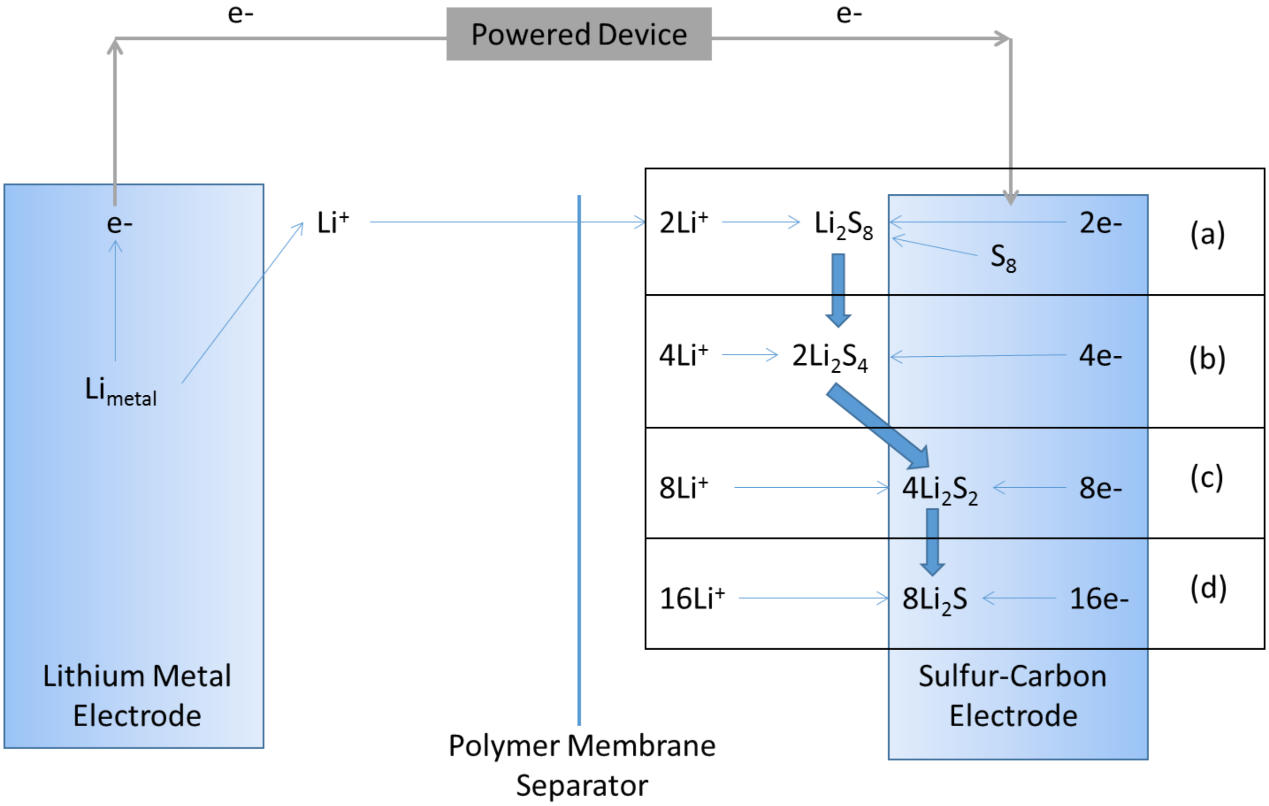

Figure 2: Example sequence of reactions during discharge of Li-S electrochemical cell. PS species (Li_2S_n) can have a variety of n values. All reactions for soluble species ($n > 2$) occur during PS adsorption on the electrode surface, while insoluble species ($n < 2$) remain on the surface after reaction.

2.3 Polysulfide Shuttling and Sulfur Migration

Undesired side reactions within batteries can have a significant impact on energy storage, overall efficiency, and power output[13]. For Li-S systems, battery performance is primarily hindered by the PS shuttling process[13]. PS shuttling occurs during the charge process (Figure 3), and results in poor coulombic efficiency by releasing thermal energy. The electrolyte fills the cell[14], ionically connecting the anode and cathode, allowing the PS to diffuse throughout the cell. As the cell is being charged, sulfur is oxidized at the cathode, and Li^+ ions are reduced at the anode. Specifically, short PS species are elongating (e.g. $2\ Li_2S_4 \rightarrow Li_2S_8 + 2Li^+ + 2e^-$) and ultimately oxidized to elemental sulfur (Reverse of equations 3-7). While full oxidation of the PS to elemental sulfur is desired, long PS chains can diffuse through the polymer membrane to the anode, where they are reduced to shorter PS species, releasing the chemical energy stored (Figure 3, left).

The short PS can then return to the cathode and begin the process again. This PS shuttling from one side of the battery to the other provides an alternative route for electron transfer in the cell, causing an internal energy release[13]. Input electrical energy converted to chemical energy is released as thermal energy during the redox shuttling instead of being stored[9]. Coulombic efficiency, the ratio of energy released (discharged) vs. the energy added (charged) is significantly diminished because energy consumed and released through the PS shuttling is not available during the subsequent discharge of the battery[9].

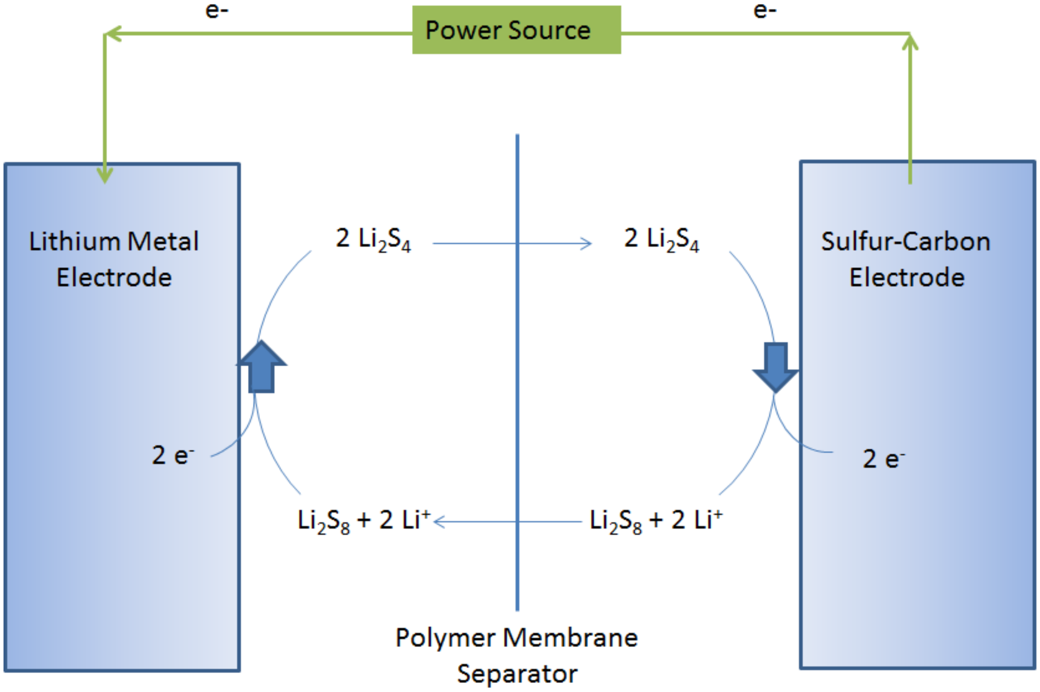

Figure 3: Example PS shuttling reactions, where long PS chains are reduced at the anode and shorter chains oxidized at the cathode, resulting in internal energy release during charging.

In addition to self-discharge caused by PS shuttling, permanent capacity loss can be caused by PS species leaving the cathode. PS in the electrolyte on the anode side of the cell is unable to undergo desired energy storage reactions. Sulfur species can also be deposited at the anode, where short PS are further reduced to insoluble Li_2S_2 and Li_2S during chargin. The deposition of these insoluble PS species results in increased resistance at the lithium metal/electrolyte interface, as well as permanent loss of sulfur, depleting the active material and decreasing capacity over time[9]. The lithium sulfide layer results in polarization of the Li anode due to the resistance of the deposit, as well as the loss of S active material from the cathode, reducing overall capacity[9]. Lithium sulfide species deposited at the anode as well as PS shuttling during charging are hurdles toward the implementation of Li-S batteries.

2.4 Carbon Material Development

Finding a way to mitigate or prevent PS shuttling is essential to building reliable and efficient Li-S batteries. The key to diminishing PS shuttling may lie in the structure of the conductive carbon material that is used in the sulfur-carbon (SC) electrode. The carbon provides two essential properties to the electrode – it facilitates electron transfer and increases the surface area for the sulfur adsorption[15]. Sulfur is a poor conductor of electrons, with an electrical conductivity of 10^{-15} S/m [16]. If a pure sulfur electrode was used, electrons would not be able to travel to the current collector and through the external circuit. By incorporating a porous carbon structure, such as carbon black, the electrons used during discharge and charge reactions with the elemental sulfur are able to conduct through the electrode (amorphous carbon has a conductivity of 10^{3} S/m, compared to 10^{-15} S/m for elemental sulfur[16,17]). The high porosity of the carbon structures used also allows high surface area loading of the sulfur, which keeps the total thickness of the sulfur low and minimizes the resistive losses due to electron transfer through the sulfur during charge/discharge[18,19]. If sulfur is in large clumps in the electrode due to insufficient carbon black content, most of the sulfur would be unable to react with the electrolyte[20]. With a carbon support, the sulfur can be loaded on the high surface area of the carbon through melt impregnation (sulfur melts at 115 °C, well below any reaction temperatures for the carbon support). The high surface area increases sulfur available for reaction and provides a surface for soluble PS species to adsorb, react, and deposit insoluble species.

Because the carbon additive plays such a crucial role in the performance of the battery, designing a new carbon material may improve on the conductivity and solubility challenges Li-S faces. By rational design of a carbon structure, we can tune different properties of the material, such as porosity, surface area, conductivity, and/or morphology to maximize the positive effects on the Li-S chemistry. The conducting carbon will have very specific features, each playing an important role in the behavior of the battery.

First, we propose to use carbon with an inverse opal macrostructure. Inverse opals have high surface areas and periodic structures[21,22]. The high surface area allows diffuse sulfur distribution. The ordered structure provides uniform, continuous paths for electron transport. Finally, large pores facilitate lithium diffusion through the electrode. Inverse opal carbon (IOC) structures have many uses, including quantum dot solar cells[23], liquid crystal displays[24], and supercapacitors[25], and can provide valuable qualities in Li-S systems as well. Figure 4 shows an IOC, fabricated by filling the interstitial space in colloidal crystals with carbon precursor and the subsequent decomposition of spherical polymeric colloidal particles to produce the structure below[18].

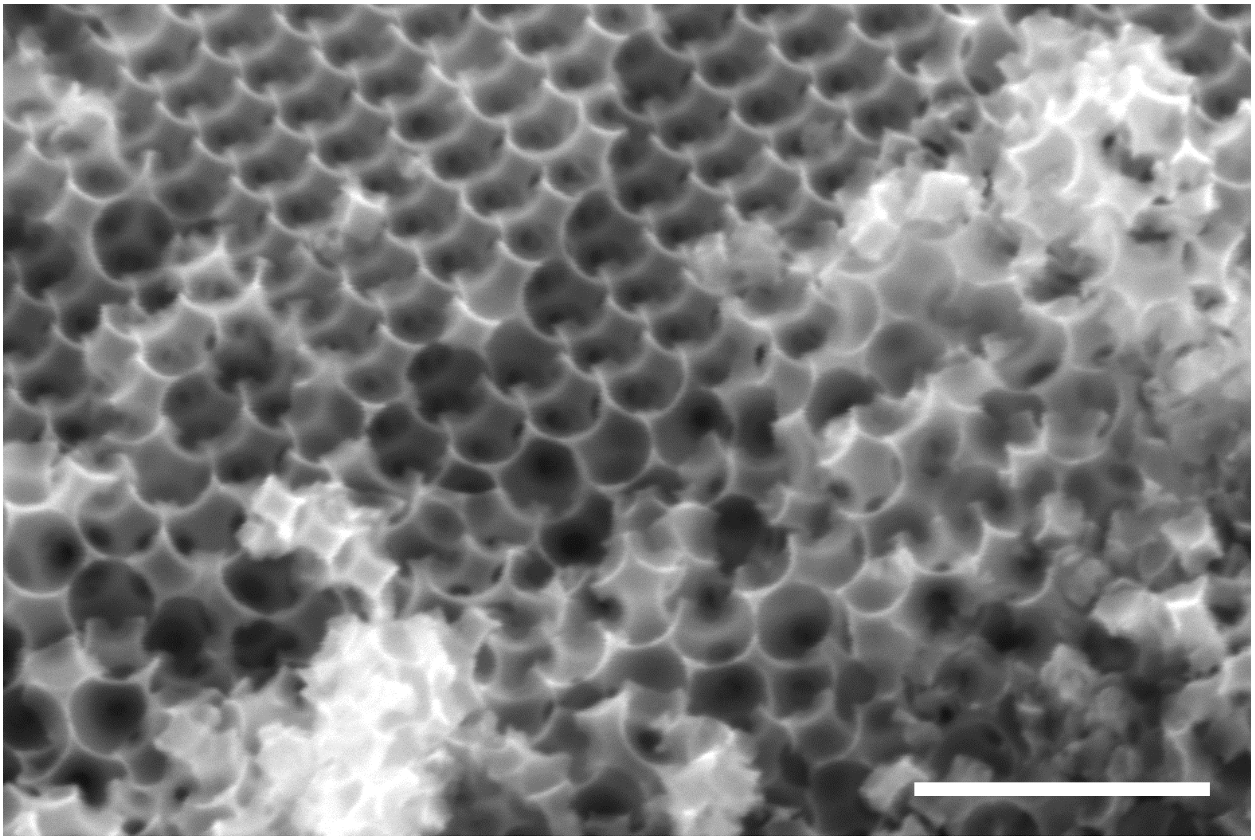

Figure 4: Scanning electron micrograph of inverse opal carbon. Scale bar 1 µm.

In addition to an inverse opal macrostructure (100 –1000 nm), we propose to incorporate meso/micropores (1 –20 nm) within the inverse opal macrostructure. Through the use of pluronics, nanotubes with tunable diameters can be incorporated into the carbon macrostructure[26]. Pluronics are a type of surfactant that produce mesoporous and microporous structures under specific conditions[26,27]. The intent of incorporating these smaller pores is to promote a size exclusion effect to mitigate the formation of soluble PS species. The hypothesis is that during the sulfur impregnation step, only shorter sulfur species will physically be able to move into the tubes and be deposited on the carbon. If only shorter sulfur species are available for reaction, the reduction process should bypass longer, soluble PS species and be directly converted to the insoluble Li_2S and Li_2S_2 species. By limiting the production of soluble, longer PS chain intermediates, the loss of sulfur through PS shuttling will be decreased or eliminated. The microporous property of the new material is the most important, as it has the largest impact on improving the performance of the battery.

Having both micro- and macroporous elements in the conductive carbon will provide the optimal environment for desired operation of the Li-S battery. The meso-/micro pores will implement size exclusion principles, while the large IOC structure will provide a reliable conductive medium and structured porous structure to promote ion diffusion. Limiting PS shuttling will diminish the effects of both self-discharge and poor coulombic efficiency[9].

3. Sulfur Sublimation

3.1 Introduction

The interface between elemental sulfur and conductive carbon additives plays an important role in the overall performance of Li-S batteries. Due to sulfur's poor electrical conductivity, electron transfer required for desired electrochemical reactions is facilitated by direct contact between the sulfur and electronically conductive carbon material, and, conversely, prohibited by thicker regions of elemental sulfur[16]. Maximizing the interfacial area between the carbon and sulfur will improve overall capacity because more of the sulfur will be accessible for electrochemical reactions as opposed to forming large clumps when there is less carbon surface to spread onto. We propose the implementation of a sulfur sublimation technique to eliminate sulfur clumps and improve performance. The sulfur sublimation treatment entails exposing the sulfur-carbon (SC) electrode to elevated temperature and decreased pressure to expedite and control sulfur loss through sublimation. Controlled sulfur sublimation will remove sulfur less tightly adhered to the carbon electrode, and we hypothesize the sulfur sublimed would be from larger clumps which are electrically isolated and not available for desired electrochemical reactions, thus the sublimation treatment would be expected to improve overall electrochemical performance.

3.2 Materials and Methods

3.2.1 Electrode Fabrication and Sulfur Sublimation

Two electrodes were prepared for these experiments, 36 wt% sulfur and 18 wt% sulfur. For the 36 wt% electrode, 0.5 g of carbon black (Super P) and 0.5 g sulfur (Sigma Aldrich) were ball milled in a planetary mill at 800 RPM for 5 minutes twice using 1 mm zirconia beads. The SC mixture was then heated at 155 °C for 10 hours. The material was ground in a mortar and pestle for 10 minutes to break up the clumps. 0.33 g of the SC mixture was mixed with 0.2 g carbon black and 1 g 12 wt% polyvinylidene fluoride (PVDF) in n-methyl-2-pyrrolidone (NMP). The slurry was mixed in a centrifugal mixer for 5 minutes and cast on aluminum foil using a 200 µm doctor blade. The electrode was dried overnight at 70 °C. The initial sulfur and carbon content was changed to 0.25 g S and 0.75 g carbon black for the production of the 18 wt% S electrode.

Sulfur sublimation in completed electrodes was conducted in a vacuum oven at 70 °C. Each electrode (punched with die to 1.6 cm^2 disk) was first weighed, and then left in the vacuum oven between 1 and 3 hours. After the specified amount of time, the electrodes were removed from the oven and weighed again. All mass loss was assumed to be from sulfur sublimation. Control experiments performed under identical conditions to those used to sublime sulfur for electrodes fabricated without sulfur had negligible mass loss after extended heating, suggesting that mass loss due to other components in the electrode, including any adsorbed water, was not significant.

The electrode disks were used as the cathode in CR-2032-type coin cells fabricated in an argon glove box (<1 ppm O_2 and H_2O). The electrolyte was prepared in advance by mixing 1.30 g dimethyl ether (DME) and 1.59g 1,3-dioxolane (DOL) in a scintillation vial, followed by dissolving 0.572 g lithium bis(trifluoromaethane) sulfonamide (LiTFSI) in the mixture, producing 1 M LiTFSI in 1:1 DME/DOL by volume. Lithium metal was used as the anode, trilayer polymeric membranes from Celguard used as the separator, and 1 M LiTFSI in 1:1 DME/DOL was used as the electrolyte.

3.2.2 Cycling

Coin cells were tested electrochemically using a MACCOR cycler. Each test was started on a discharge, cycling 5 times galvanostatically at each C rate of charge/discharge, 0.1 C, 0.2 C, 0.5 C, 1.0 C and 2.0 C, followed by 50 cycles at 0.1 C. 1C was assumed to be 1675 mA/g sulfur in the electrode and the current was adjusted depending on the amount of sulfur in the electrode. The potential window during cycling was restricted to 1.55 to 3.5 V (vs. Li/Li+).

3.3 Results and Discussion

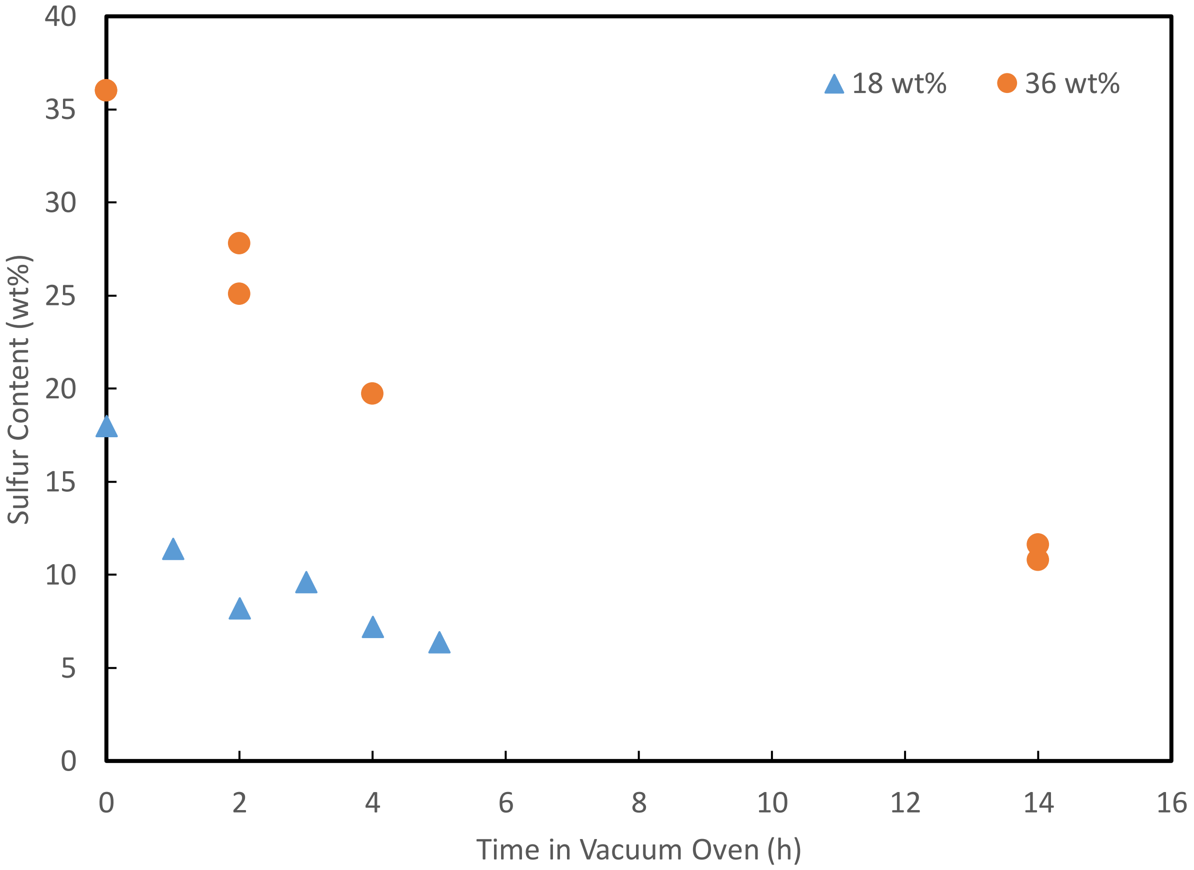

Figure 5: Sulfur mass as a function of time in vacuum oven for electrodes that initially contain 18 (blue circles) and 36 (orange circles) weight percent sulfur.

Elemental sulfur begins to sublime at 43.5 °C under atmospheric pressure[28]. During typical battery electrode preparation, the drawn electrode slurry thin film (consisting of a mixture of sulfur, carbon, PVDF, and NMP) is exposed to 80 °C for 12 hours to evaporate the NMP solvent, and then placed in a vacuum oven for a minimum of three hours[29]. Of these two steps, the first cannot be removed because the NMP needs to be evaporated from the electrode material or else it will diffuse into the electrolyte during cell assembly and impact the electrochemical properties of the Li-S battery. To determine if the vacuum drying step induced sulfur sublimation, a series of electrodes were exposed to varying times in the vacuum oven. The results (Figure 5) show a substantial sulfur loss in under an hour, with continued loss after as long as 14 hours. Using the data to extrapolate exact sulfur loss over time, the amount of sulfur removed from the electrode can be controlled.

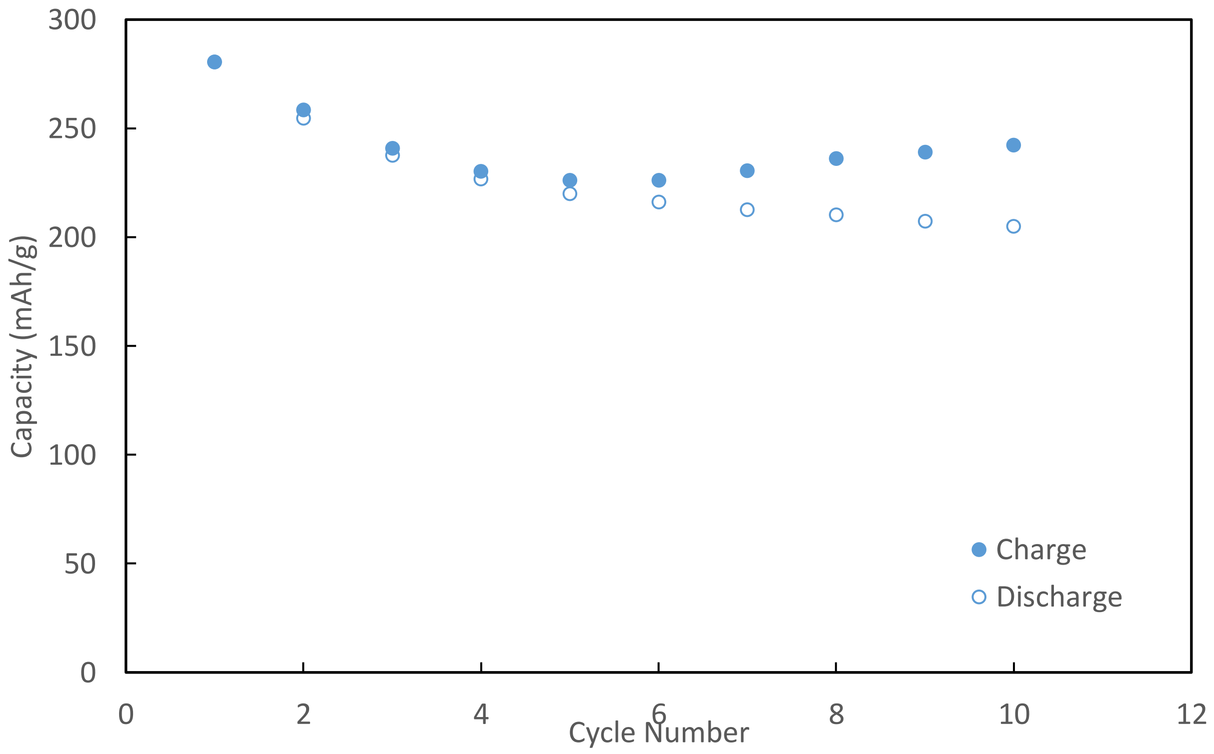

Figure 6: Cycling performance of Li-S battery electrode that underwent vacuum drying before cycling. 36 wt% sulfur cathode, cycle rate 0.05 C.

While the loss of sulfur from the electrodes was initially problematic, it was observed the coulombic efficiency (Figure 6) was near 100% in the first few charge/discharge cycles. This is not typically observed in Li-S systems, where some capacity on the charge cycle is typically lost to driving PS shuttling instead of chemical energy storage, decreasing the coulombic efficiency. One explanation for the behavior is the sublimation of sulfur from the electrode limited polysulfide shuttling, increasing the coulombic efficiency. As we will discuss later in Section 5, decreasing the total amount of sulfur in the electrode increases coulombic efficiency by limiting the concentration of PS species in the electrolyte, decreasing the available species to participate in shuttling.

The sublimation of sulfur from the electrodes may provide additional positive coulombic efficiency effects. By subliming some sulfur, large clumps of sulfur on the surface could be reduced or eliminated, leaving sulfur evenly distributed on the surface. A thin, well distributed layer of sulfur on the surface would be conducive to desired electrochemical reactions, electrically by minimizing insulating effects of sulfur. Areas of thick or globular sulfur would provide large electrical resistance, inhibiting reduction during discharge; however a thin layer would allow more sulfur to be electrically connected with the carbon black, promoting reduction and oxidation on the respective cycles. To investigate this behavior, controlled amounts of sulfur were removed via sublimation from the electrodes using the vacuum oven (e.g. subliming sulfur from 36 wt % to 20 wt %), and then compared with control electrodes originally Figure 7 shows a comparison between an electrode originally prepared with 18 wt % sulfur, and an electrode originally prepared at 36 wt % sulfur that was reduced to 20 wt % through sublimation. Contrary to our hypothesis, the performance of sublimed electrodes was worse than electrodes originally prepared at the specified sulfur content. The coulombic efficiency of the sublimed electrode was significantly lower at C/10, and 5-10% lower at higher cycle rates. The discharge capacities were also lower in the sublimed electrode.

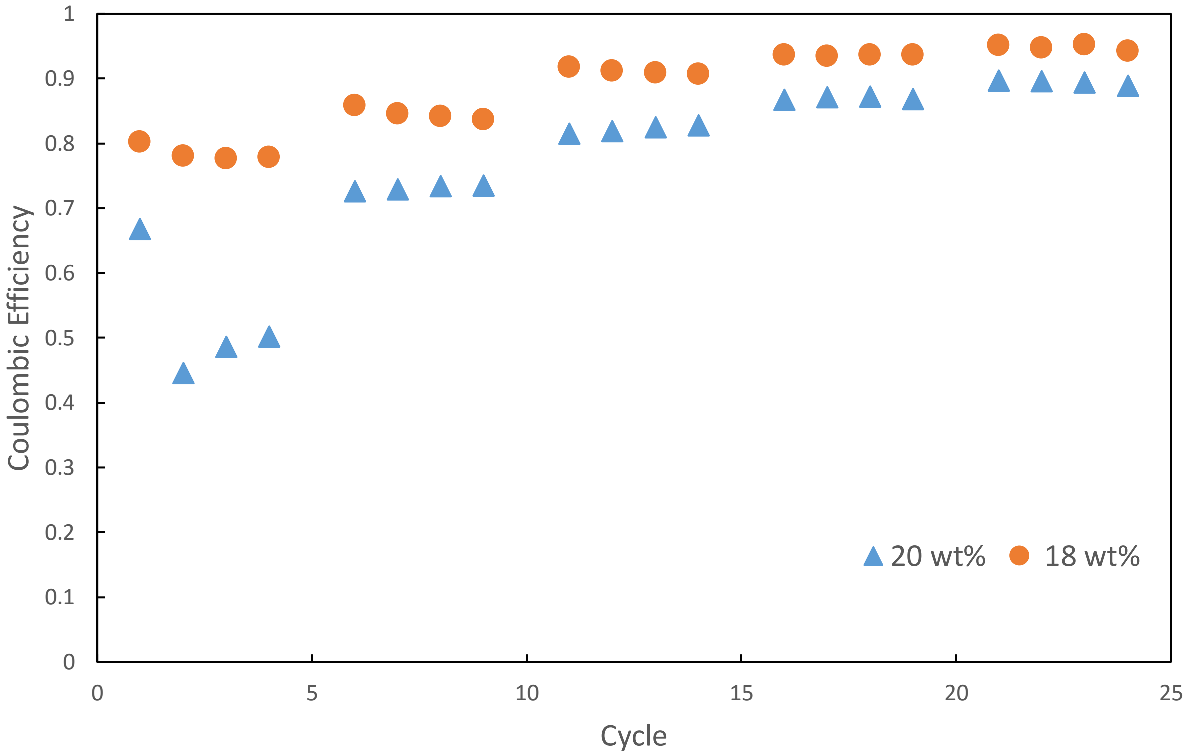

Figure 7: Coulombic efficiency of sample prepared at 18 wt% S (orange circles) and sample that underwent sulfur sublimation treatment with a final 20 wt% S (blue triangles).

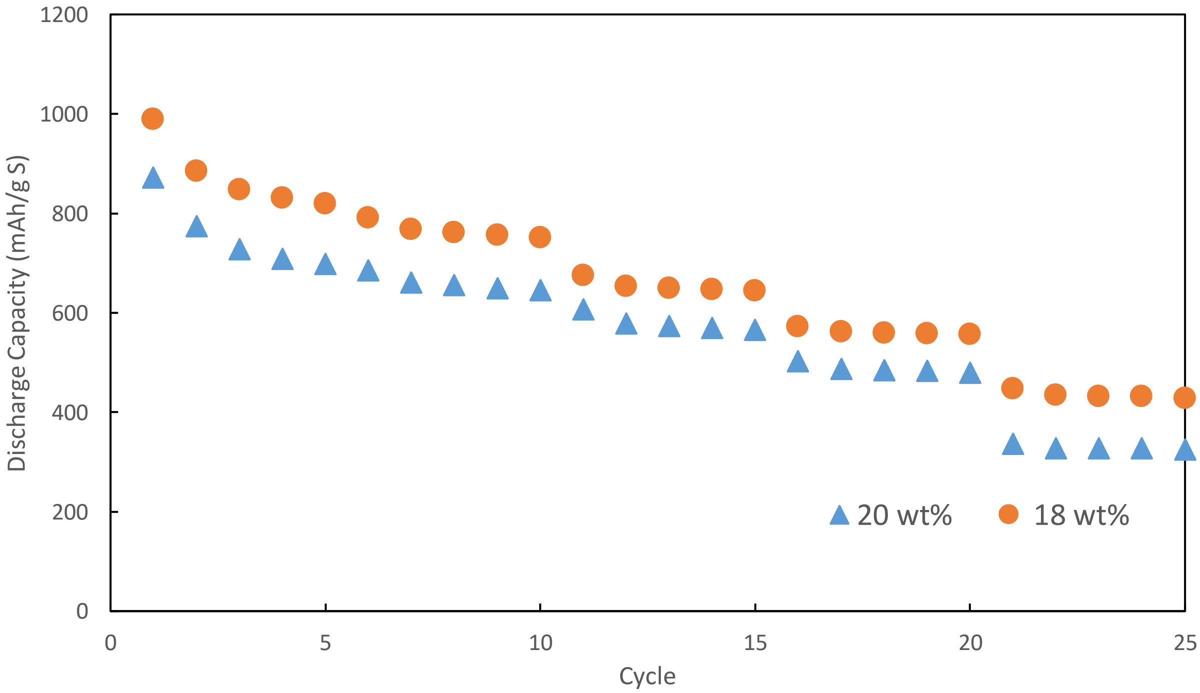

Figure 8: Discharge capacity of sample prepared at 18 wt% S (orange circles) and sample that underwent sulfur sublimation treatment with a final 20 wt% S (blue triangles).

The experimental results show the sublimation process did not improve the coulombic efficiency or capacity of the batteries. Several possibilities might explain the observed behavior. First, the sublimation process may have not been as selective as desired in the removal of electrically insulating clumps of sulfur. If the thin layers of sulfur were removed preferentially to the thicker clumps, it would negatively impact the capacity. Thin regions of sulfur are more reactive and we hypothesize it constitutes a majority of the capacity in the cell, the electrically insulated sulfur clumps remaining largely inert[30].

3.4 Conclusion

Li-S electrodes were fabricated and exposed to low temperature and pressure to sublime elemental sulfur. The electrochemical performance of these electrodes were compared with the performance of control electrodes. While the initial hypothesis was the sublimation treatment would positively impact electrode performance, the experimental electrodes performed no better than control electrodes. The sulfur removed during the sublimation treatment was either non-detrimental or valuable in the effective performance of the electrode, instead of hindering performance through insulating layers or unused active material as we predicted. While sulfur loading plays an important part of making Li-S batteries viable, modification through directed sulfur sublimation appears fruitless. However, this work demonstrates sulfur sublimation is an important consideration when developing fabrication procedures and conditions, as sulfur can easily sublime during procedures generally taken for granted during already-implemented industrial manufacturing settings-.

4. Sulfur Loading

4.1 Introduction

The composition of the battery electrode is important in tuning the overall performance. The active material component of the electrode is directly involved in the electrochemistry of the battery and is responsible for the amount of energy stored in the battery. Traditional cathode materials for Li-ion batteries contain metal oxides, which allow storage and release of lithium ion species through intercalation. The amount of active material is proportional to the amount of energy that can be stored. For Li-S battery applications, elemental sulfur serves as the active material. During discharge, elemental sulfur, S_8, is reduced through redox reactions with Li^+ in the electrolyte and e^- from the external circuit (delivered through the conductive additive). This process produces PS that are soluble in the electrolyte. Further reduction of the PS in the electrolyte produces shorter and shorter PS species, until insoluble Li_2S_2 and Li_2S are deposited on the carbon surface in the electrode. Further energy can be released through the reduction of Li_2S_2 species to Li_2S.

The total amount of sulfur active material in the electrode plays a vital role in battery performance. Several effects are at play as the total sulfur content in the electrode is modified. First, increasing the sulfur content in the electrode increases total capacity, as more material is present to undergo desired redox reactions. Conversely, as the amount of sulfur is increased, the overall cathode will have reduced electronic conductivity due to the poor conductivity of sulfur[16]. A balance between sulfur content and the amount of electrically conductive material (i.e. carbon black) is needed. In these experiments, the effects of sulfur content in the cathode on the capacity and coulombic efficiency will be explored, where the initial sulfur loading into the SC material is varied via the initial impregnation amounts, and any sublimation is avoided to the extent possible (e.g., no vacuum treatment) during electrode processing.

4.2 Materials and Methods

4.2.1 Electrode and Cell Fabrication

To prepare a 9 wt% S electrode, 0.125 g of sulfur was combine with 0.875 g carbon black (Super P) and ball milled (planetary ball mill, Fritsch) two times at 800 RPM for five minutes, with a 30 minute rest between cycles. The carbon/sulfur mixture was heated at 155 °C for 10 hr. in a glass scintillation vial covered with a watch glass. The SC mixture was ground in a mortar and pestle for 5 minutes. 0.33 g of the carbon/sulfur mixture was mixed with 0.02 g carbon black and 1 g 12 wt% PVDF in NMP. The slurry was mixed in a centrifugal mixer for 5 minutes, and then film coated on aluminum at 200 µm thickness using a doctor blade. The slurry was dried overnight at 80 °C. To prepare electrodes with different sulfur loadings, the initial sulfur/carbon ratio was increased to 25, 33, 50, and 75 wt% S, producing 18, 25, 36, and 52 wt% S loading in the final electrodes respectively.

Electrode disks were punched using a 14 mm diameter die, producing 1.6 cm^2 discs. The electrodes were incorporated into CR-2032-type coin cells in an argon glove box (<1 ppm O2 and H2O). The electrolyte was prepared in advance by mixing 1.30 g DME, 1.59 g DOL and 0.572 g LiTFSI, producing 1 M LiTFSI in 1:1 DME/DOL by volume. Lithium metal was used as the anode, trilayer polymeric membranes from Celgard used as the separator, and 1 M LiTFSI in 1:1 DME/DOL was used as the electrolyte.

4.2.2 Coin Cell Testing

Coin cells were tested electrochemically using a MACCOR cycler. Each test was started on a discharge, cycling 5 times galvanostatically at each C rate of charge/discharge, 0.1 C, 0.2 C, 0.5 C, 1.0 C and 2.0 C, followed by 50 cycles at 0.1 C. 1 C was assumed to be 1675 mA/g sulfur in the electrode and the current was adjusted depending on the amount of sulfur in the electrode. The potential window during cycling was restricted to 1.55 to 3.5 V (vs. Li/Li+).

4.2.3 Materials Characterization

Scanning electron microscopy (SEM, Quanta 650) was used to image electrode morphology, and energy dispersive spectroscopy (EDS SEM, Quanta 650) was used for elemental analysis and mapping of electrodes.

4.3 Results and Discussion

To examine the effect of sulfur content and performance of Li-S batteries, five different loadings, 9,18,25,36, and 52 wt% S, were prepared and electrochemically evaluated. To improve overall quantitative results and ensure thorough appropriate statistics to reach each conclusion, each loading was represented by multiple electrode preparations and at least four separate half cells (batteries prepared with lithium metal anodes and the cathode material fabricated in the lab).

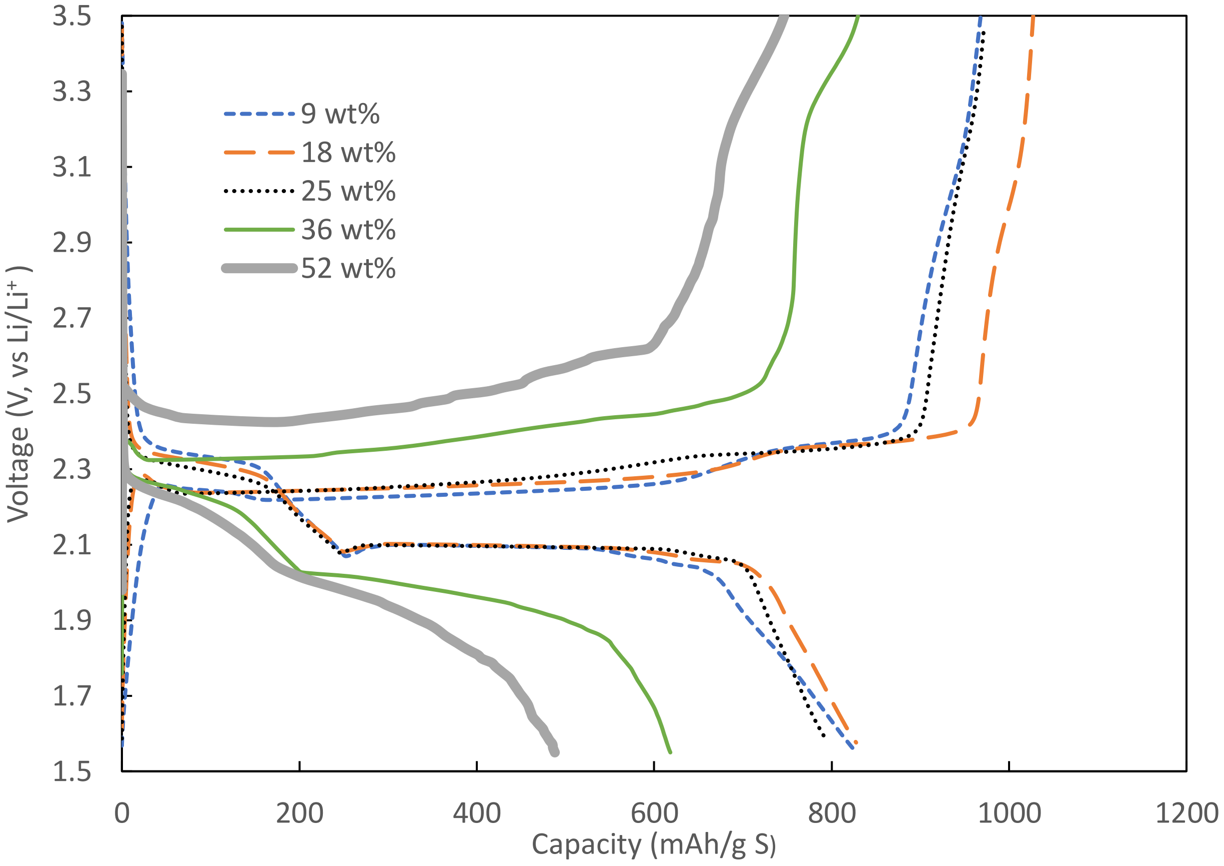

Figure 9: Charge/discharge profiles at different sulfur loadings at a rate of 0.1 C.

Overall electrode gravimetric capacity was observed to decrease as the total weight fraction of S in the electrode increased. Figure 9 shows representative charge/discharge voltage profiles of the various Sloadings at C/10 (165 mA/g S). Viewing these representative voltage profiles shows several trends as the sulfur/carbon ratio is increased. First, as the sulfur content increased, the difference between the average potential of charge/discharge increased. Overpotential, or the difference between the thermodynamic electrochemical reaction potential and the actual charge/discharge potential, thus was increasing with increased S loading[31]. Under ideal conditions, charge and discharge would occur at the same potential (or series of potentials in the case of the Li-S reaction mechanism). A widening in the voltage gap between charge and discharge represents the overpotential as the polarization increases for both processes. The overpotential increase with higher sulfur content shows a loss of energy efficiency in the system which is likely lost in form of heat. Several factors can impact and exacerbate overpotential, including charge carrier depletion at the electrode surface (concentration overpotential)[32] and interface or membrane effects (resistance overpotential)[33]. For Li-S systems, thicker layers of sulfur in the cathode provide an electrically resistive barrier, contributing to overpotential and overall decrease in cell efficiency. Secondly, as the rate of charge/discharge was increased, overall capacity decreased. The decrease in capacity was likely limited by a combination of electron transfer and mass transfer limitations. As the ratio between sulfur and the conductive carbon material was increased, less surface area is available for the necessary PS oxidation and reduction reactions during charge and discharge. In addition, because the sulfur inhibits electron transfer, thick layers and clumps of sulfur prevent full utilization of the active material; if sulfur is not in electrical connection with the carbon (and more specifically electrons from the external circuit), it cannot participate in the desired electrochemical reactions without dramatic polarization.

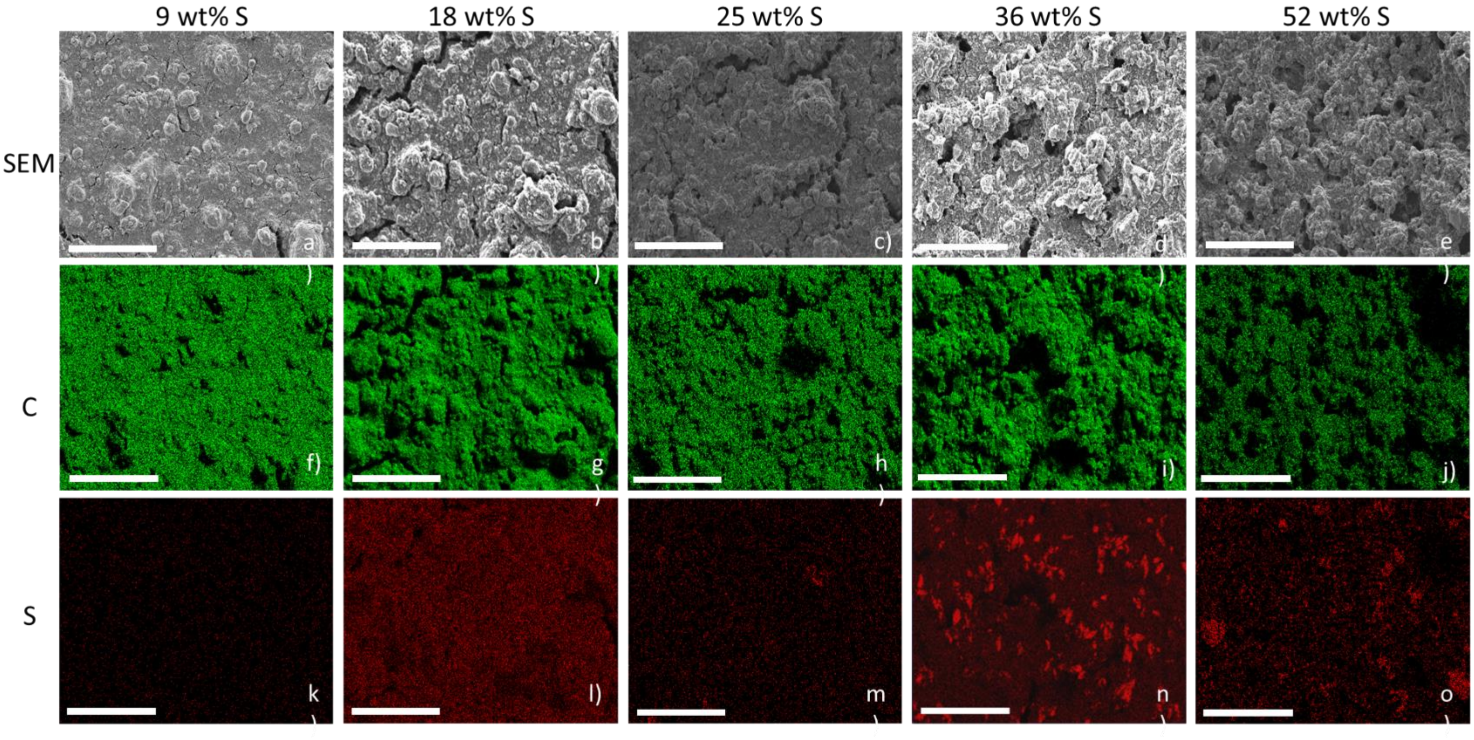

Figure 10: SEM (top row) and EDS of carbon (middle) and sulfur (bottom) of carbon-sulfur electrodes. (Scale bar: 400 µm)

Sulfur distribution in the carbon support of the electrodes plays an important role in the overall performance of the battery. EDS was used to provide compositional mapping of the electrodes. Figure 10 shows SEM and EDS SEM images of electrodes at 9, 18, 25, 36, and 52 wt% sulfur. At this scale, we can make observations about the macroscopic distribution of the components of the electrode. The carbon black (middle row) is distributed evenly throughout the sample image.

Several trends in Figure 10 give us insight into why different loadings result in different electrochemical performance. At lower weight percentages, the sulfur appears to be evenly distributed, but also rather sparse in the electrode. As the sulfur content increases, the sulfur signal becomes stronger, but also becomes more heterogeneous, even at this macroscopic level. At 52 wt% S, the electrode has large (1-10 µm) clumps of sulfur and is not evenly distributed throughout the electrode. These two trends can be compared with electrochemical performance of the electrodes with different loadings. First, at lower sulfur loadings, the high coulombic efficiency can be associated with an abundance of carbon substrate for the sulfur to adhere to and react with during charge and discharge. As the sulfur/carbon ratio increases, we see a decrease in coulombic efficiency.

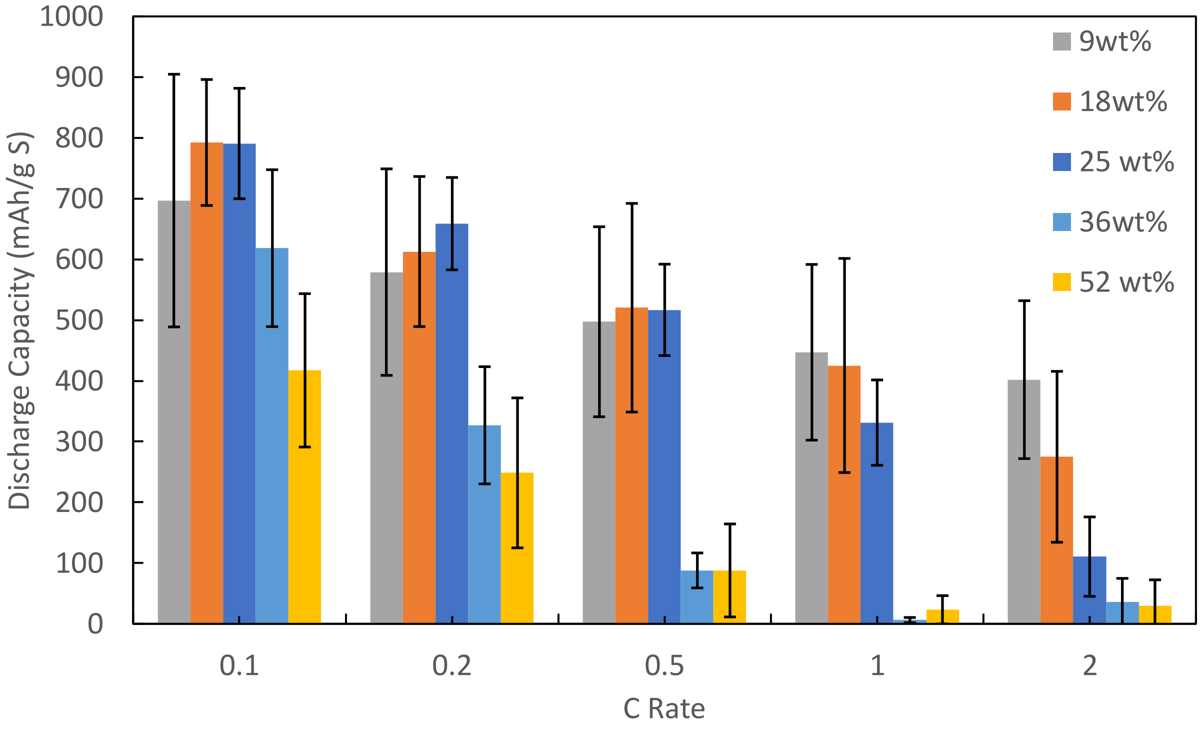

Figure 11: Average gravimetric discharge capacity as a function of C rate and sulfur content. Error bars represent the standard deviation of a minimum of 4 electrodes and 20 cycles were used for each C rate and electrode loading.

Gravimetric capacity (energy stored normalized by the mass of active material with units mAh/g S) was significantly impacted by the sulfur content of the cathode. Figure 11 shows a small increase, followed by a large decrease in capacity as the sulfur wt% is increased. The drop in capacity as sulfur content increases can be related to the sulfur distribution in the electrode. As sulfur content increased, larger masses of sulfur occupied the electrode. The images (Figure 10n and 10o) of electrodes with high sulfur content show large concentrations of sulfur, as well as large S aggregates. Large clumps of sulfur cause electrical isolation from the conductive carbon, preventing the desired electrochemical reactions. Therefore, any sulfur electrically isolated will not contribute to the overall capacity, lowering the gravimetric capacity of the cell. The electrochemical performance and observed sulfur distribution suggest, at a certain point, increasing the sulfur to carbon ratio will only result in sulfur clumping and not significantly contribute to the capacity of the cell.

In an effort to better analyze the results of the sulfur loading experiments, the sulfur/carbon ratio was normalized by the surface area of the carbon material resulting in an average sulfur thickness in nanometers (Figure 13, orange squares). Because the sulfur/carbon interface is crucial to the desired redox reactions, sulfur thickness should serve to be a metric that can be compared across not only our materials, but also with other Li-S battery experiments. Figure 12 compares the initial discharge gravimetric capacity of the half cells to the thickness of the sulfur in nm with other values from literature.

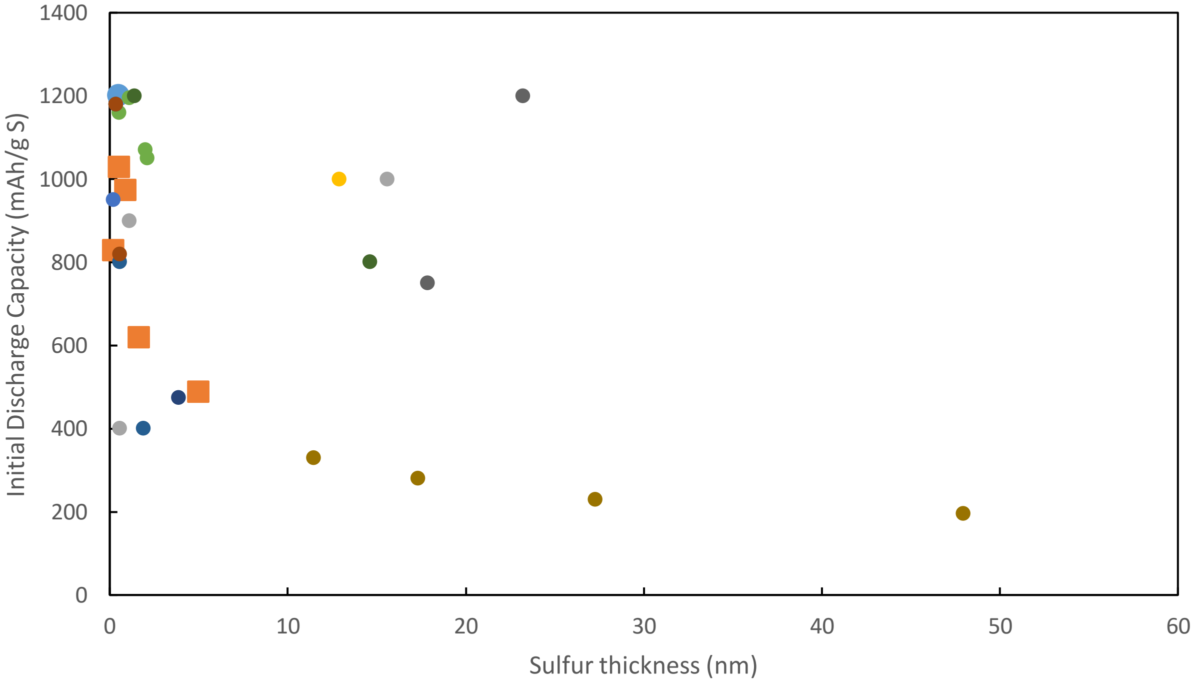

Figure 12: Initial gravimetric capacity vs. average sulfur thickness for our results (orange squares) and a variety of literature sources[34–42].

As the thickness of sulfur on carbon support in the cathode increases, the gravimetric capacity decreases quickly, resembling an exponential decay. Electrical resistivity is directly related to the thickness of the sulfur, having a greater impact from thick layers of sulfur. At C/10, the voltage drop due to sulfur resistivity is less than 0.06 V for 5 nm layers of sulfur, but the linear increase with sulfur thickness contributes a 0.6 V drop at 1 C, drastically impacting the overpotential on charge and discharge as well as the power output of the cell. Figure 13 shows the voltage drops at varying C rates using carbon black as the current collector ($62\ m^2/g$).

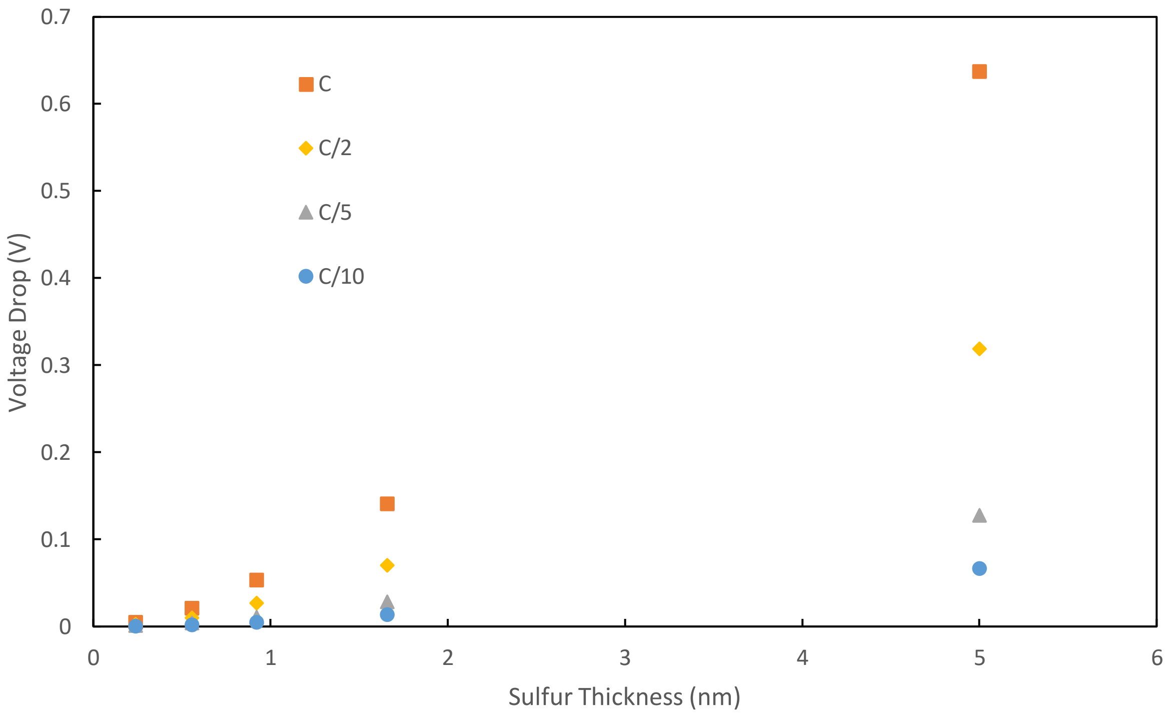

Figure 13: Estimated voltage drop (V) due to electron conductivity through the sulfur layer vs. S thickness (nm) at different C rates.

4.4 Conclusions

A rigorous study of sulfur loading and its effect on coulombic efficiency and overall capacity of Li-S electrodes was conducted. Results show increased sulfur loading has initial benefits before becoming detrimental to discharge capacity. Coulombic efficiency was highest for low sulfur loadings, but did not considerably drop off until 36 wt% loading. EDS was used to observe the sulfur distribution in the electrode, and showed a change from evenly dispersed to clumped sulfur with increased content. By applying a simple normalization of sulfur loading through calculating average sulfur thickness, we compared the general performance of many materials and batteries tested in the literature, showing an inverse relationship between average sulfur thickness and discharge capacity.

5. Polystyrene Particle Synthesis

5.1 Introduction

The structure and morphology of the conductive carbon additive is a major area of research in the pursuit of making Li-S batteries a viable replacement for conventional Li-ion technologies[9]. Tuning the morphology, on macro-, meso- and microscopic scales, has been pursued to diminish PS shuttling and increase overall capacity of the cells. IOC structures are honeycomb-like materials with close packed spherical chambers on the order of 100 to 1000 nm[21]. These structures provide a high surface area and porosity along with an interconnected electronically conductive matrix conducive to improved Li-S battery performance.

To this end, IOC materials were implemented by Agrawal. et al., and initial findings reported achieving 1600 mAh/g capacity (95.5 % of the maximum theoretical capacity) on initial discharge, though capacity decayed dramatically within 50 cycles[18]. The group reported differences in electrochemical performance when the carbon matrix had voids of 740 vs. 490 nm IOCs. In our work, we hypothesize the size of the IOC pores could substantially affect the performance of the battery via impacts on the mass transport of Li ions within the electrode pores. To examine these effects in more detail, PS particles of varying sizes were needed to template the size of the IOC macroporous structures.

Polystyrene particles have many applications, including paints[43,44], biomedical materials[45], and optics[46]. Polystyrene particle fabrication have been widely studied, and many synthesis procedures are reported in the literature[47–51]. For our application, monodisperse particles were desired to determine the size effects of voids in the carbon matricies templated by these particles Li-S battery performance.

5.2 Materials and Methods

Colloidal polystyrene particles (300-500 nm) were synthesized using procedures adapted from literature[49]. Styrene (Sigma-Aldrich, *ReagentPlus*, with 4-tert-butylcatechol as stabilizer, ≥ 99.0%) was pretreated using a prepacked column (Sigma-Aldrich, Inhibitor, prepacked column for removing tert-butylcatechol) to remove the polymerization inhibitor. In a typical synthesis, a three neck 500 mL round bottom flask was filled with 290 mL DI water and 8.86 g styrene and heated to 70˚C in an oil bath and allowed to thermally equilibrate for 30 minutes. Next, 0.204 g potassium persulfate (Sigma-Aldrich, ACS reagent, ≥ 99.0%) was added to catalyze the styrene polymerization reaction. The head space was purged with nitrogen and flowed at 1 mL/s for the duration of the experiment. The two phase system was stirred for 8.5 hours with a magnetic stir bar, resulting in a final milky white suspension. Styrene concentration was used to control particle size; increases in initial styrene content increased average particle size.

A zetasizer (Malvern) was used to determine particle size distributions for the polystyrene particles. A scanning electron microscope (SEM, FEI Quanta 650) was used to image particle size and morphology.

5.3 Results and Discussion – Particle Synthesis

Polystyrene particles play a large role in the fabrication of IOC, and large quantities are needed for small samples of IOC material. Based on literature procedures, we aimed to produce monodispersed polystyrene particles of varying diameters (100 – 500 nm). We hypothesized that by increasing the available styrene in the reaction vessel, while maintaining constant amounts of initiator and water, particle diameter would increase. By keeping the initiator mass constant over the different syntheses, we limited new particle formation and instead increased particle size via the addition of more styrene.

The reactor vessel was agitated at a constant rate during the particle synthesis. Due to the similar quantities of styrene and water, which are minimally miscible, agitation was required to increase the liquid-liquid interface and promote particle synthesis.

A variety of particle sizes were produced. As anticipated, the particle size, measured using dynamic light scattering (DLS), increased as the initial monomer concentration was increased in the reactor. In addition to varying particle size batches, monodisperse particle populations are desirable. Polydispersity (PDI) is a measure of the distribution of particle sizes, governed by the equation:

$$PDI = \left(\frac{width}{mean}\right)^2 \tag{6}$$

a dimensionless value where the width is the peak width and the mean is the mean particle size. This definition is used in DLS measurements as opposed to being defined as PDI = Mw/Mn. A PDI of less than 0.1 is considered monodisperse. In the case of all of our batches of particles, the PDI values are less than 0.1, implying monodisperse distributions at all sizes.

Styrene Mass (g)	**Diameter (nm)**	**Yield**	**PDI**
2.99	187	0.73	0.05
8.96	279	0.76	0.04
11.95	315	0.76	0.04
23.89	511	0.80	0.07
29.90	445		0.11
35.85	510	0.86	0.08
59.73	529	1.00	0.06

Table 1: Yield and PDI for seven batches of spherical polystyrene particles.

Further analysis of the particle characteristics demonstrate a clear connection between particle size and the initial amount of monomer. For all experiments, the amount of initiator was kept constant. As particle size increases, the mass follows as the volume * density;

$$m = \frac{4}{3}\pi r^3 \rho \tag{7}$$

where r is the radius of the particle, ρ is the density of the polystyrene, and m is the mass of the individual particle. The equation is a simple model of particle growth, and allow us to determine average particle size from initial styrene content. For the model, a range of particle diameters are used to determine individual particle mass, which is then multiplied by the average number of particles from the experimental batches, giving a theoretical "initial styrene content" based on size. This theoretical curve is plotted with the actual data in Figure 10. While the intricacies of the particle growth are more nuanced, this simple model implies the particles grow after an initial number of nuclei are created, which makes sense because a set amount of initiator was used for all syntheses, as opposed to continuing to increase the number of particles as the polymer continues to lengthen.

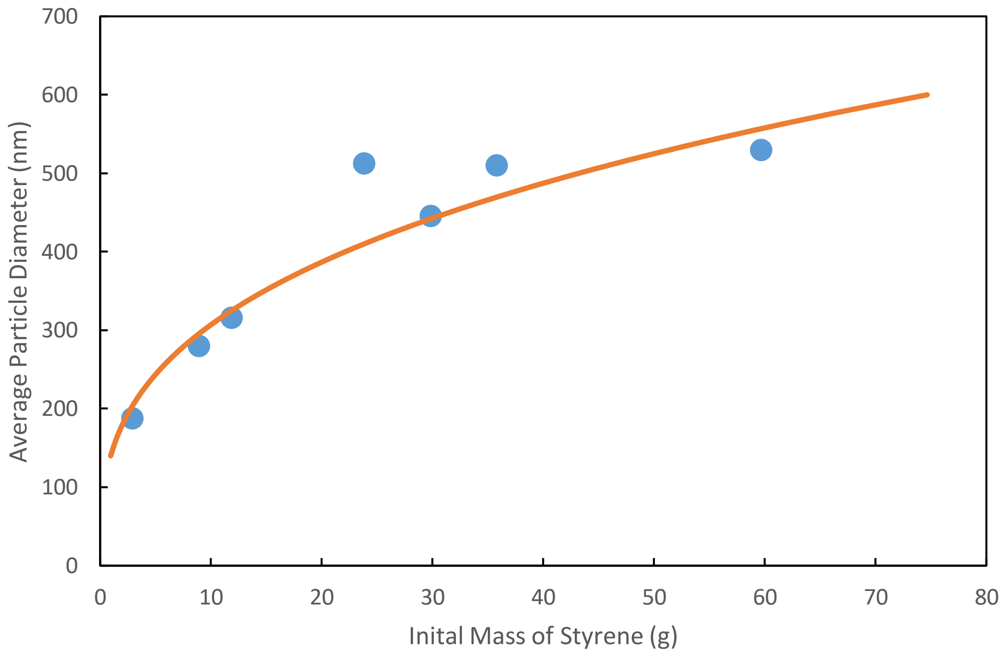

Figure 14: The average particle diameters plotted against the initial styrene content (blue circles) and simple model relating initial mass and particle diameter governed by Eq. 7.

5.4 Conclusion

We were able to fabricate monodisperse polystyrene particles with a variety of particle diameters by varying the initial amount of styrene reagent. All particle sizes had a PDI of 0.1 or less, and product yield was above 90%. The monodisperse particles formed colloidal crystals easily, and were implemented in inverse opal materials and Li-S batteries. Particle size follows trend predictions based on even particle ripening.

6. Inverse Opal and Pluronic Templated Carbon Materials

6.1 Introduction

The sulfur-carbon interface is very important for the performance of Li-S batteries. Carbon black is a well characterized material and is helpful in preliminary studies on sulfur loading, but is ultimately limited by its internal porosity and surface area. Theoretically, using a carbon material with higher porosity and increased surface area would allow a higher sulfur/carbon ratio while maintaining a thin (<1 nm) layer of sulfur.

A variety of materials have been previously studied, including graphene[52–54], carbon nanotubes[55–57], carbon-coated microparticles[58], and IOC structures[18,59]. With a periodic structure, high porosity, and high surface area, IOCs show promise in implementing Li-S battery chemistry. Inverse opal carbon is prepared by creating colloidal crystals, in our case out of 200-500 nm diameter monodisperse spherical polystyrene particles. A resin is introduced into the interstitial spaces between the polystyrene particles after packing the sphere into a close-packed crystal, and the resin then cured. Heat treatment of the resin-impregnated crystal results in decomposition and removal of the polystyrene particles and carbonization of the resin, producing an "inverse" of the opal crystal formed with the polystyrene spheres[21]. The periodic morphology and increased surface area should improve electron conduction and Li^+ diffusion, and reduce mass transfer limitations of the Li-S reactions.

Templated carbon materials can also be pursued to address the problematic PS shuttling and improve the coulombic efficiency of the Li-S system. PS shuttling during charging allows some energy to be released through internal redox reactions, instead of being stored with the desired sulfur oxidation. Microscopic carbon tubes (1-5 nm) can provide additional improvements to the Li-S system. By confining the sulfur and Li-S species in small tubes, PS species would either be unable to diffuse away from the carbon structure in the cathode, or may be more directly converted from S by avoiding S_8 species to insoluble PS species[15]. Reducing the amount of PS species available for diffusion out of the electrode will limit coulombic losses. Pluronic templated carbon structures are one proposed route to provide the desired structures. Pluronics are surfactant molecules that can assemble into multi-molecular structures. Some pluronics assemble into cylinders on the order of 1-10 nm, within the desirable range for containing and confining the PS species. The pluronic assemblies are combined with resin and carbonized at elevated temperatures, producing a carbon structure with small tubes of uniform size throughout the material. Ultimately, combining the IOC with pluronic templated nanotubes may provide the best of both templated length scales in the same material and have an important impact on Li-S batteries.

6.2 Materials and Methods

6.2.1 Colloidal Opal Assembly

Colloidal opal crystals were assembled using polystyrene particles fabricated in procedures described previously (Section 5.2). First, the particles were washed to remove excess styrene reagent and other impurities using the following procedure. 10 mL of particle suspension was added to a centrifuge tube and centrifuged for 2 hr at 6000 RPM. The particles are concentrated in the bottom of the tube but have not formed a pellet yet. The top 7 mL of the supernatant was removed with a pipette, DI water was added to replace the removed liquid, and sonicated to return the particles into a suspension. These steps were completed again to ensure only polystyrene particles remained.

The washed particle suspension was centrifuged for 1 hr at 6000 RPM, concentrating the particles in the bottom of the tube. The top 7 mL of supernatant were removed, and the sample sonicated to disperse the particles in the remaining solution. The sample was centrifuged again for 1 hr at 6000 RPM, producing a colloidal crystal pellet. The supernatant was removed, and the crystal allowed to dry in ambient air conditions for two days. The final crystal was white, brittle, and slightly opalescent.

6.2.2 Inverse Opal Carbon Fabrication

To begin IOC fabrication, a resin precursor solution was prepared. In a typical synthesis, 1.101 g resorcinol (ACS reagent, ≥ 99%) was dissolved in 2.16 g formalin (formaldehyde solution, 37 wt% in water, contains 10-15% methanol as stabilizer). 12 µL of 20 wt% NaOH solution was added to the resorcinol/formalin solution to promote polymerization of the resin. The colloidal crystal was immediately added to the precursor solution and allowed to soak overnight. The following day the crystal, which had broken up into large pieces during the soaking process, was removed from the solution, and forced air was used to remove excess liquid. The now pinkish resin-impregnated colloidal crystal was cured at 80 and 120 °C for 24 hours each.

Next, the resin-impregnated crystal was placed in a ceramic crucible and fired in a tube furnace under 1 mL/s N_2 gas flow. The firing procedure is as follows: a 1°C/min ramp to 400 °C, a 2 hr hold at 400 °C, a 5 °C/min ramp to 850 °C, and finally a hold at 850 °C for 3 hr, followed by ambient cooling to room temperature. The product was a black, slightly opalescent material. The carbonized IOC was ground in a mortar and pestle for 20 minutes, large particles separated using a 37 µm sieve, and the ground again for 30 minutes. This process ensured large particles sizes did not negatively influence electrode preparation.

6.2.3 Electrode and Cell Fabrication

50 wt% IOC impregnated sulfur (S/IOC) was prepared by mixing 0.5 g IOC with 0.5 g sulfur (Sigma-Aldrich) in a mortar and pestle for 20 minutes, then heated at 155 °C for 10 hrs. A 36 wt% S electrode was prepared by mixing 0.33 g of 50 wt% S/IOC with 0.02 g carbon black (Super-P) in a mortar and pestle. The mixture was placed in a mixing capsule, and 1 g of 12 wt% of PVDF in NMP was added as a binder. The slurry was mixed for 10 minutes at 500 rpm, and then coated on aluminum foil using a slurry coater and 200 µm doctor blade. The electrode film was dried at 70 °C overnight and the final dry product was kept in a desiccator. Sulfur content in other variations was controlled by initial mixture of sulfur and IOC.

The electrode was punched into 1.6 cm^2 discs for coin cell preparation. Coin cells were fabricated in an argon glove box (<1 ppm O_2 and H_20). Lithium metal was used as the anode, 1 M LiTFSI in 1:1 DME/DOL was used as the electrolyte, and trilayer polymeric membranes from Celgard were used as the separator.

6.2.4 Pluronic Templated Carbon Fabrication

Pluronic templated carbon (PTC) fabrication began by preparing a solution of 4.5 mL ethanol (Sigma-Aldrich) mixed with 4.5 mL 3 M HCl (Sigma-Aldrich) in a 20 mL scintillation vial. 1.1 g of resorcinol and 1.1g Pluronic F-127 (Sigma-Aldrich, powder) were added to the solution and shaken by hand until dissolved. 1.3 g formalin was added to the solution. The viscous solution sat for 1 hr, producing a gel-like material and supernatant solution in the vial. The sample was centrifuged at 100 rpm for 50 minutes in a glass centrifuge tube to concentrate the pluronic structure from the excess liquid. The supernatant was removed, and the sample allowed to dry in air overnight. The supernatant solution was removed, and the resin-soaked pluronic structure was allowed to dry overnight. The sample was cured at 80 and 120 °C for 24 hours each. The cured, resin-infused pluronic structure was placed in a ceramic crucible and placed in a tube furnace. The furnace procedure was as follows: starting at room temperature, 1 °C/min ramp to 400 °C, hold at 400 °C for 2 hr, 5 °C/min ramp to 850 °C, hold at 850 °C for 3 hr, and finally allowed to cool to room temperature. The sample was ground in mortar and pestle for 20 minutes to make a final black powder.

6.2.5 Analytical Testing – Raman, Surface Area and Pore Analysis, SEM

Raman spectroscopy was used to determine surface compositional information and carbon molecular morphology, SEM (FEI Quanta 650) was used to image IOC material, and BET surface area and pore size analysis (Quantachrome NOVA 2200e) was used to determine pore size, surface area, and void space, and image measurements were conducted using ImageJ.

6.3 Results and Discussion

6.3.1 Inverse Opal Carbon

Toward the goal of practical implementation of Li-S batteries, we have developed procedures for producing IOC, pluronic carbon (PLC) materials, and inverse opal pluronic carbon (IOPLC). First, two IOC materials were fabricated using 280 nm and 390 nm particles. The surface area was measured using the Brunauer-Emmett-Teller (BET) method, and pore volume was measured using the Barrett-Joyner-Halenda (BJH) method. The 390 nm IOC had a surface area of 400 m^2/g, and 0.05 cm^3/g of pore volume. The 280 nm IOC had a surface area of 690 m^2/g, and 0.22 cm^3/g pore volume. Both of these materials have a surface area much higher than the Super P carbon black at 62 m^2/g, providing an increased conductive interface support for sulfur in the cathode material. While a majority of the pore volume observed on both materials falls under 5 nm pore radius (Figure 15), the pores only constitute 50% of the sulfur volume at 36 wt% S. For confirmation of IOC formation, SEM micrographs were obtained for the two materials (Figure 17). The honeycomb like structure is produced from the removal of polystyrene particles during firing. For the 280 nm IOC, the pores were smaller than the template at around 200 nm, which is either a result of inaccurate particle measurements or shrinking effects during firing. Finally, Raman spectroscopy was used to observe the carbon molecular structure. Carbon generally exhibits two peak wavenumbers, and the peak value reveals carbon bonding information. The peak values of 1591 and 1397 correspond to the transition between crystalline carbon (graphene) and nanocrystalline graphite[60].

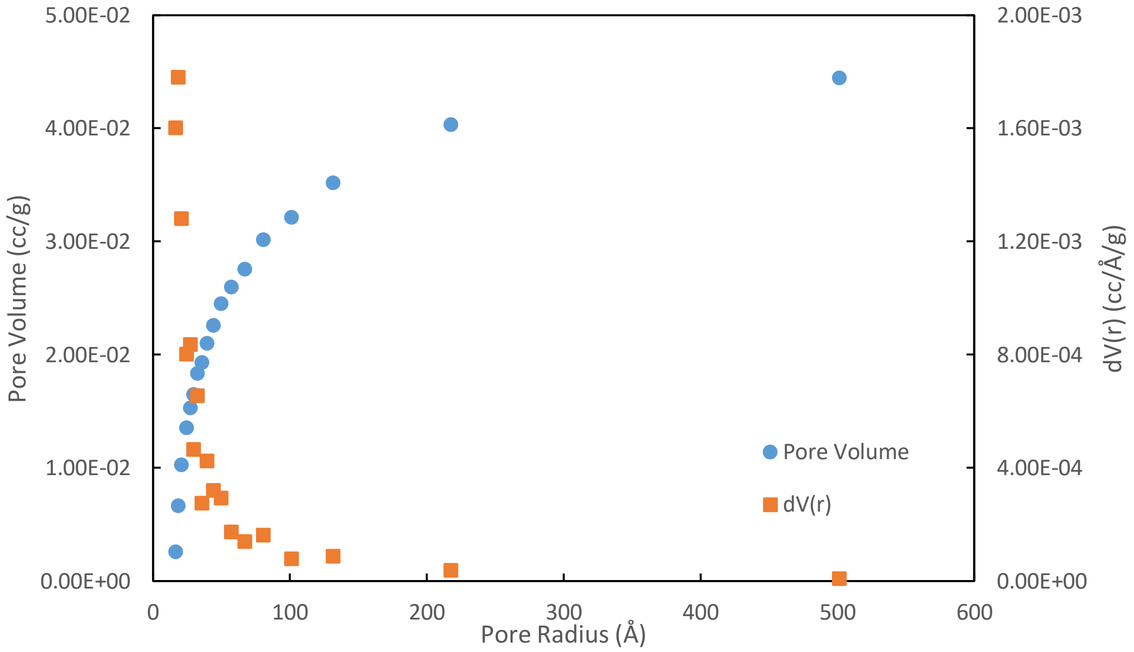

Figure 15: IOC-390 BJH data, Pore volume (blue circles) and dV(r) (orange).

For electrochemical testing, 370 nm IOC was prepared using 370 nm particles and used as the carbon material in a cathode with a loading of 36 wt% S. The performance of the electrode material (Figure 16) was compared with the performance of one of the carbon black electrodes prepared at the same loading. While the performance is relatively similar, there are some important differences. At low C rates (0.1 C and 0.2 C) the IOC electrode exhibits improved coulombic efficiency. Additionally, this test shows the IOC material performs at least as well as carbon black, and should serve as a suitable support for more intricate carbon materials.

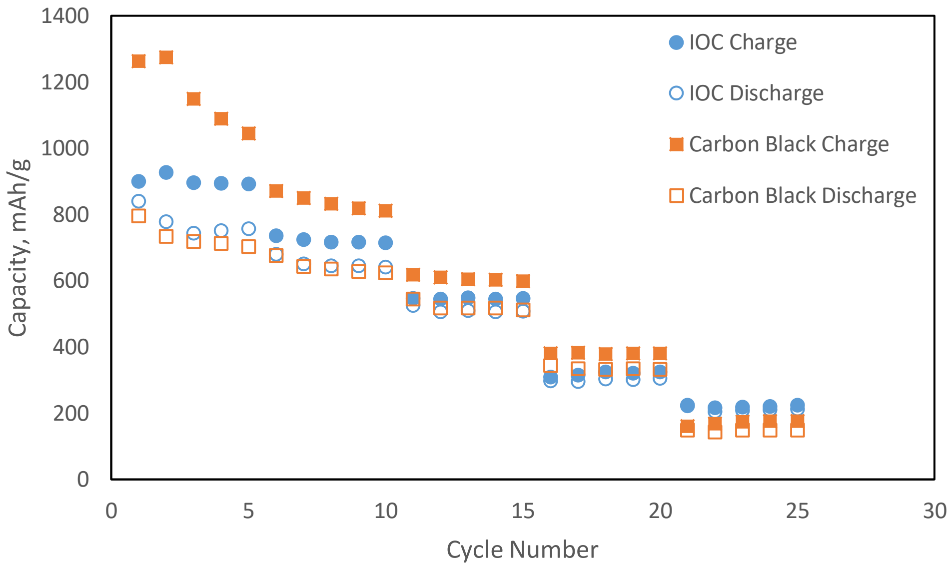

Figure 16: Rate capability comparison between Carbon Black and Inverse Opal electrode performances. Electrodes were cycled 5 times at each C rate: 0.1, 0.2, 0.5, 1, and 2 C

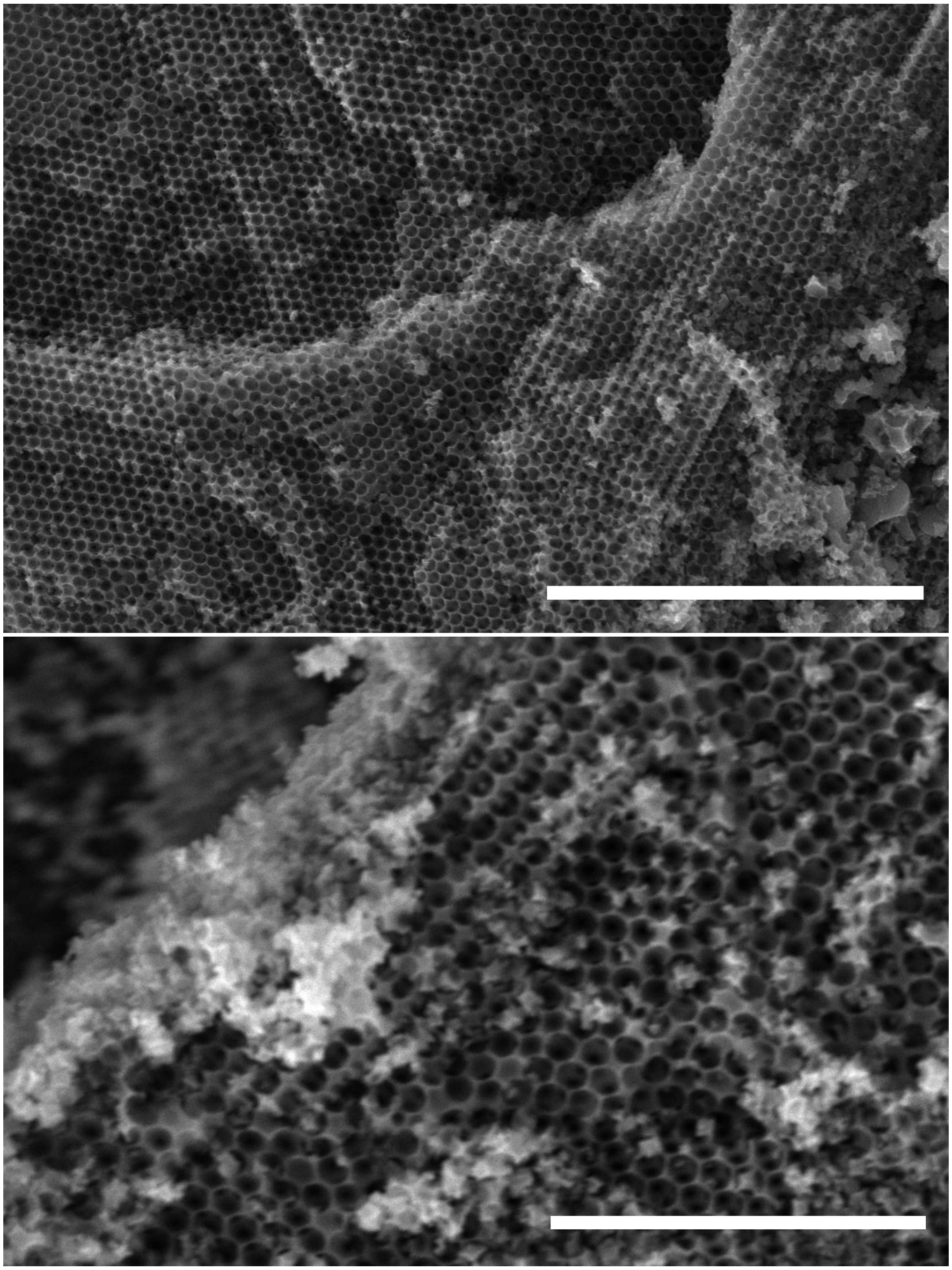

Figure 17: IOC-270 (top) and IOC-390 (Bottom). Scale bars 5 µm.

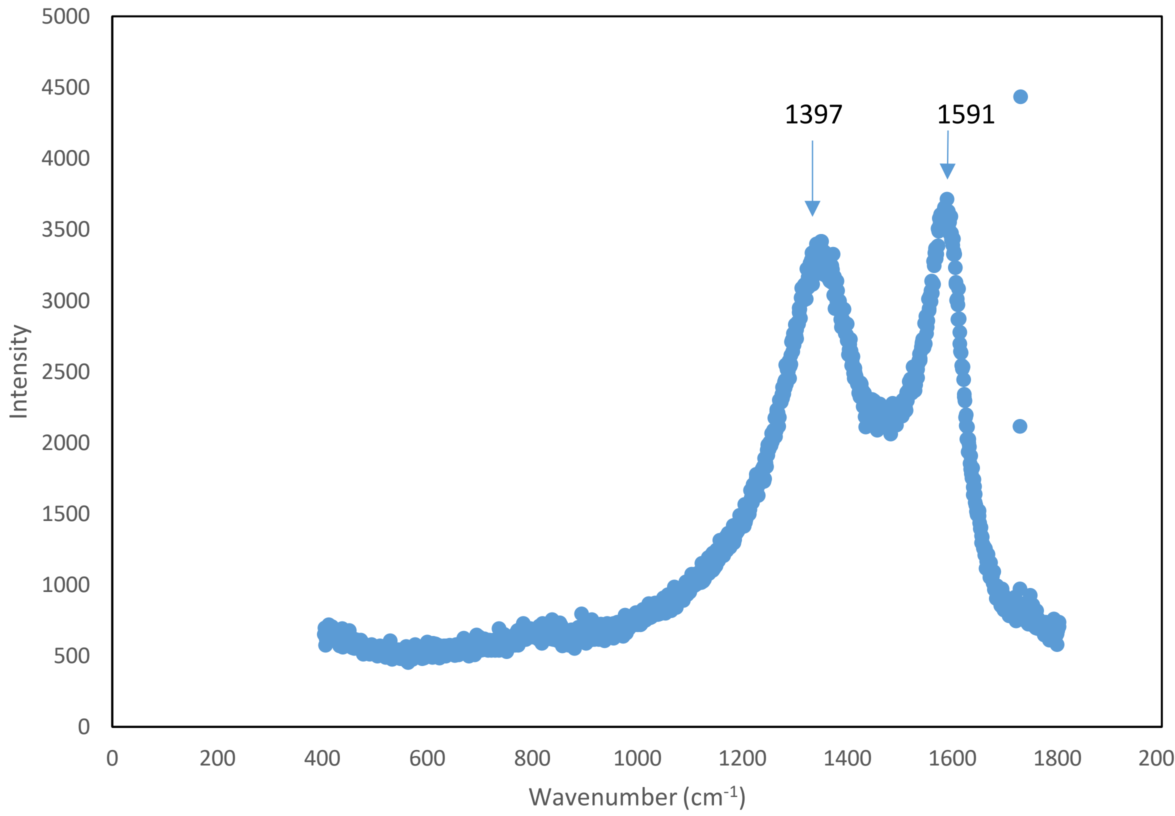

Figure 18: Raman spectrograph of 370 nm IOC.

6.3.2 Pluronic Templated Carbon

In an effort to prevent polysulfide shuttling through size exclusion, PLC was fabricated and analyzed. The pluronic creates nm sized rods in the resin, and during firing, the pluronic was removed and the resin was carbonized, leaving nanopores in the carbon. Using BET and BJH methods, the surface area was determined to be 490 m^2/g and the pore volume was 0.33 cm^3/g. The formation of carbon nanopores with a radius of 3 nm was confirmed in the BJH pore volume data (Figure 19), where the dV(r) peak around 30 Å. A peak in the dV(r) plot represents a large gradient in the pore volume. Additionally, the majority of the pore volume measured is observed under 50 nm. Raman spectroscopy was used to determine carbon morphology (Figure 20). The results are similar to the IOC (Figure 18), a result of the same resin precursor. The peaks and intensity magnitudes are consistent with nanocrystalline graphite. The separation of the lower peak (1357 and 1441 cm^{-1}) could be a result of residual pluronic material that was carbonized instead of being burned off. Figure 20 also exhibits a peak around 450 cm^{-1}, which results from the sulfur in this sample[61].

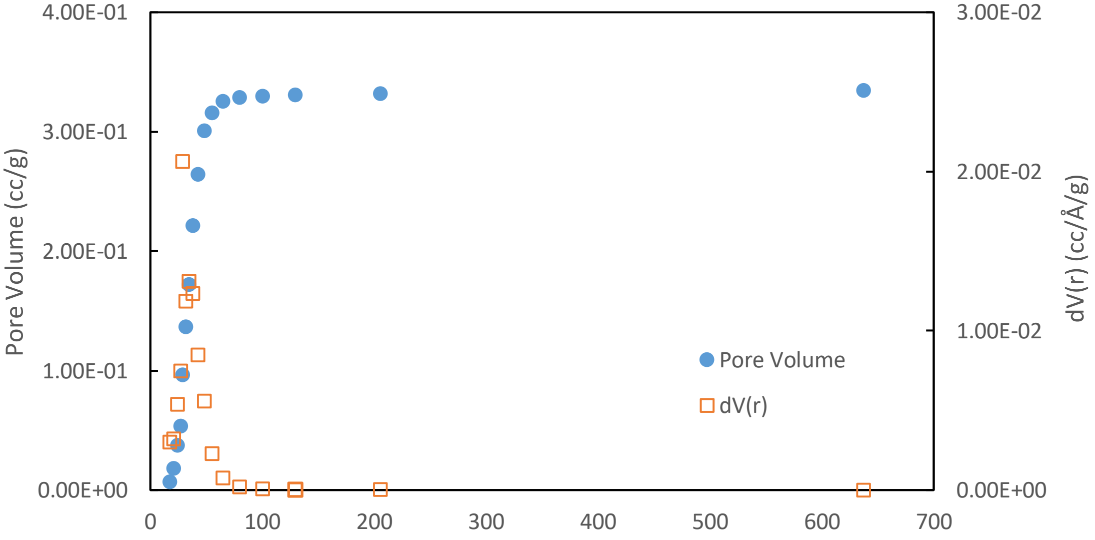

Figure 19: BJH pore volume and dV(r) of PLC.

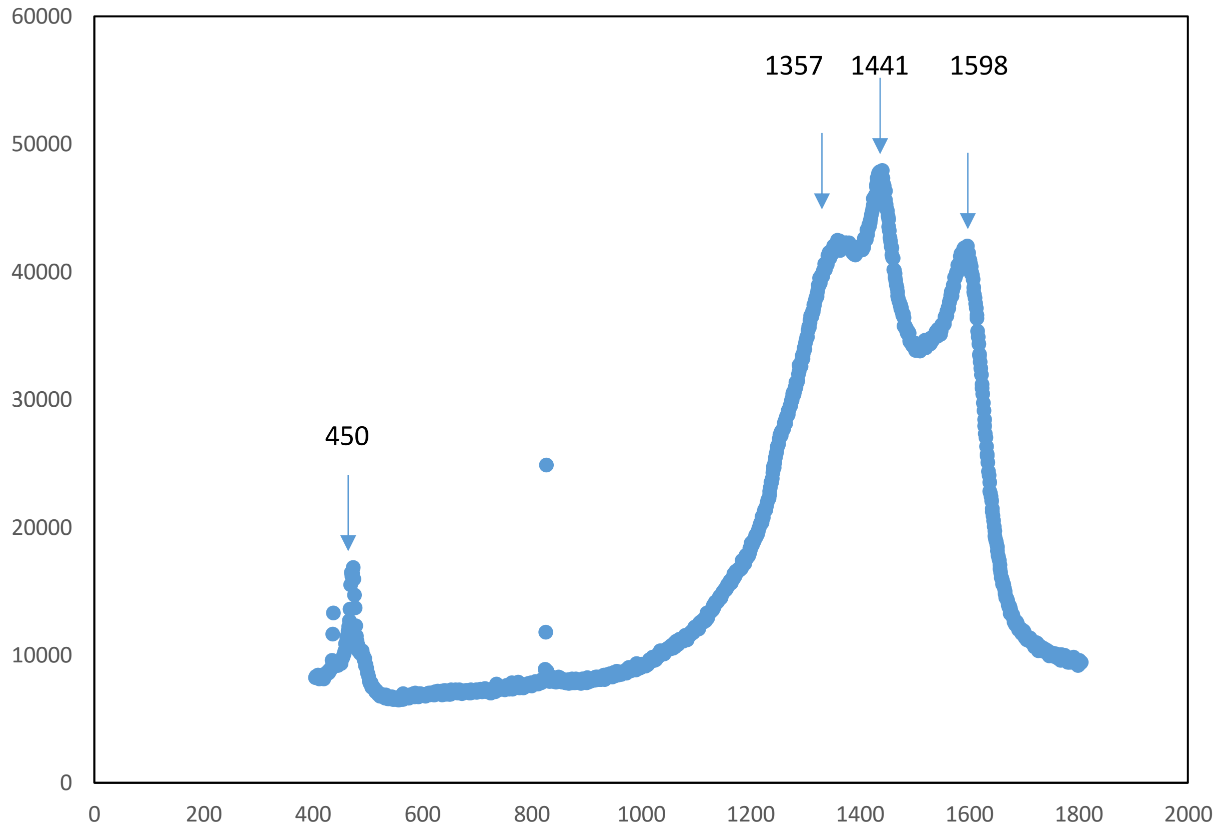

Figure 20: Raman spectrograph of PLC electrode impregnated with sulfur.

After confirming the fabrication of nanoporous carbon material, the PLC was electrochemically tested and exhibited several improvements over carbon black (Figure 21). The coulombic efficiency is higher, and there is lower polarization between the charge and discharge profiles.

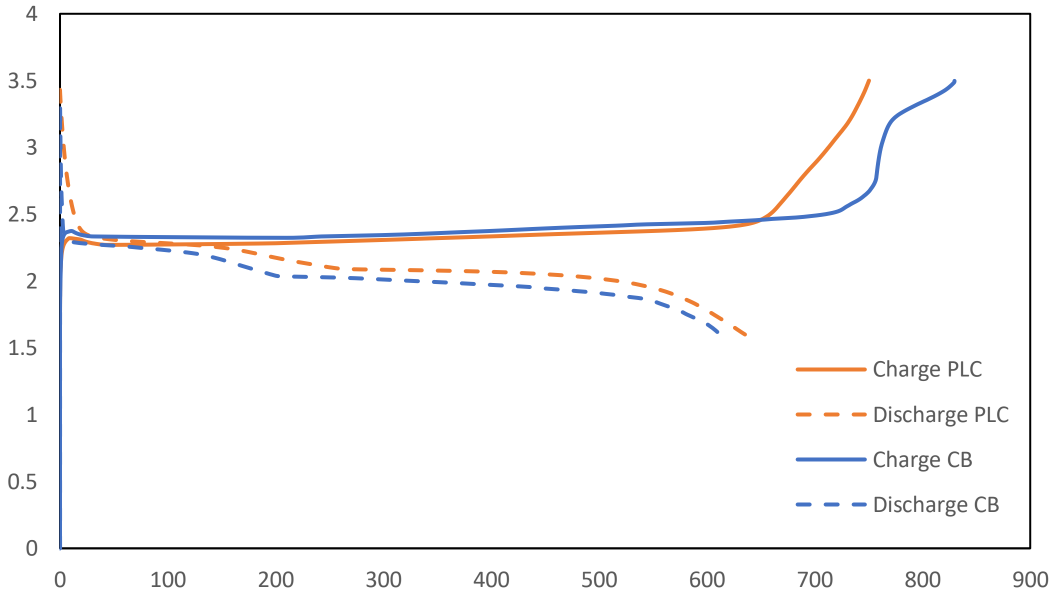

Figure 21: Voltage profiles (36 wt% S) PLC (orange) and carbon black (blue) Li-S cells.

The implementation of both IOC and PLC properties into one carbon support material proved more difficult than anticipated. Because the pluronic can produce different structures based on solution conditions, we used the same procedure as producing independent PLC. When combining the procedures, the resin and pluronic must diffuse into the interstitial spaces of the polystyrene particle opal structure. Unfortunately, the pluronic proved too viscous to reliably impregnate the opal structure. Another procedure was tested. A suspension of pluronic, resin precursor, and polystyrene particles was centrifuged to try and produce an opal crystal with other two materials already in the spaces between particles. The experiment was unsuccessful as the density of the pluronic was too high compared to the polystyrene particles, separating the two materials instead of combining them. While it is likely a solution is available, more rigorous and varied techniques may be required to produce the desired PLIOC material.

6.4 Conclusion

Initial investigation into IOC, PLC, and IOPLC materials revealed some promise as use as a carbon additive in Li-S battery electrodes. The high porosity and surface area of IOC materials provide a beneficial macrostructure component, while the PLC provides additional surface area and possible containment of PS species. Additional research is necessary to successfully combine IOC and PLC materials, and should be a future research direction.

7. Final Conclusions

A variety of lithium-sulfur (Li-S) batteries were prepared to investigate the effects of sulfur content and carbon morphology on overall performance. The performance of Li-S batteries was negatively impacted by using sublimation to reduce overall sulfur content in the electrode when compared with the control electrodes. Sulfur content observed across five different loadings showed lower loadings (9, 18 wt% S) to have high gravimetric capacities and better coulombic efficiency, but overall capacity is well below practical application. High sulfur loading (36 and 52 wt% S) showed decreased capacity and coulombic efficiency, especially at high rates, while moderate sulfur content exhibited both reasonable overall capacity as well as high gravimetric capacity and coulombic efficiency. Evaluating sulfur content through average sulfur thickness proved to be a good starting metric for determining appropriate sulfur content based on carbon support surface area, though other factors must also be investigated to achieve better Li-S battery performance.

Inverse opal carbon (IOC) and pluronic carbon (PLC) were fabricated and implemented into Li-S batteries. A range of polystyrene particle sizes were prepared via a simple polymerization procedure, yielding monodisperse, high yielding batches. The particles were used as opal templates to produce IOC, a material with high a high surface area and periodic structure. Both IOC and PLC were incorporated into Li-S electrodes, yielding promising initial results, performing as well as or better than carbon black, and exhibiting internal structures that may prove helpful with additional research. The final goal to incorporate IOC and PLC into one material proved more difficult than anticipated, and should be the focus of future research.

8. Acknowledgements

I would like to thank everyone at the University of Virginia that has made this work possible. Thank you to my wonderfully helpful and caring lab mates, Pierce Robinson, Ethan Paharik, Colin Qi, and Spring Dong. Thank you to two very helpful and dedicated undergraduate researchers, Nam Pham and Nick Brown. Thank you Dr. Gary Koenig for your helpful guidance, experience, insight, and endless patience during my time in Charlottesville.

Works Cited

1. Tarascon, J. M. & Armand, M. Issues and challenges facing rechargeable lithium batteries. *Nature* **414,** 359–67 (2001).
2. Etacheri, V., Marom, R., Elazari, R., Salitra, G. & Aurbach, D. Challenges in the development of advanced Li-ion batteries: a review. *Energy Environ. Sci.* **4,** 3243–3262 (2011).
3. Marom, R., Amalraj, S. F., Leifer, N., Jacob, D. & Aurbach, D. A review of advanced and practical lithium battery materials. *J. Mater. Chem.* **21,** 9938 (2011).
4. Nishi, Y. Lithium ion secondary batteries; past 10 years and the future. *J. Power Sources* **100,** 101–106 (2001).
5. Thackeray, M. M., Wolverton, C. & Isaacs, E. D. Electrical energy storage for transportation—approaching the limits of, and going beyond, lithium-ion batteries. *Energy Environ. Sci.* **5,** 7854 (2012).
6. Goodenough, J. B. & Kim, Y. Challenges for rechargeable Li batteries. *Chem. Mater.* **22,** 587–603 (2010).
7. Takehara, Z. Future prospects of the lithium metal anode. *J. Power Sources* **68,** 82–86 (1997).
8. Xu, W. *et al.* Lithium metal anodes for rechargeable batteries. *Energy Environ. Sci.* **7,** 513–537 (2014).
9. Zhang, S. S. Liquid electrolyte lithium/sulfur battery: Fundamental chemistry, problems, and solutions. *J. Power Sources* **231,** 153–162 (2013).
10. Ritchie, A. . *et al.* Future cathode materials for lithium rechargeable batteries. *J. Power Sources* **80,** 98–102 (1999).

11. Hagen, M. *et al.* Development and costs calculation of lithium-sulfur cells with high sulfur load and binder free electrodes. *J. Power Sources* **224,** 260–268 (2013).

12. Kolosnitsyn, V. S. & Karaseva, E. V. Lithium-sulfur batteries: Problems and solutions. *Russ. J. Electrochem.* **44,** 506–509 (2008).

13. Mikhaylik, Y. V. & Akridge, J. R. Polysulfide shuttle study in the Li/S battery system. *J. Electrochem. Soc.* **151,** A1969–A1976 (2004).

14. Scheers, J., Fantini, S. & Johansson, P. A review of electrolytes for lithium-sulphur batteries. *J. Power Sources* **255,** 204–218 (2014).

15. Zheng, G. Y., Yang, Y., Cha, J. J., Hong, S. S. & Cui, Y. Hollow Carbon Nanofiber-Encapsulated Sulfur Cathodes for High Specific Capacity Rechargeable Lithium Batteries. *Nano Lett.* **11,** 4462–4467 (2011).

16. Wolfram|Alpha. Sulfur. (2017). Available at: http://m.wolframalpha.com/input/?i=sulfur&x=0&y=0. (Accessed: 10th January 2017)

17. Sanchez-Gonzalez, J., Macias-Garcia, A., Alexandre-Franco, M. F. & Gomez-Serrano, V. Electrical conductivity of carbon blacks under compression. *Carbon N. Y.* **43,** 741–747 (2005).

18. Agrawal, M. *et al.* Porous carbon materials for Li-S batteries based on resorcinol-formaldehyde resin with inverse opal structure. *J. Power Sources* **261,** 363–370 (2014).

19. Jayaprakash, N., Shen, J., Moganty, S. S., Corona, A. & Archer, L. A. Porous hollow carbon@sulfur composites for high-power lithium-sulfur batteries. *Angew. Chemie - Int. Ed.* **50,** 5904–5908 (2011).

20. Lin, C. N. *et al.* Understanding dynamics of polysulfide dissolution and re-deposition in working lithium-sulfur battery by in-operando transmission X-ray microscopy. *J. Power Sources* **263,** 98–103 (2014).

21. Waterhouse, G. I. N. & Waterland, M. R. Opal and inverse opal photonic crystals: Fabrication and characterization. *Polyhedron* **26,** 356–368 (2007).

22. Zakhidov, a. a. Carbon Structures with Three-Dimensional Periodicity at Optical Wavelengths. *Science (80-.).* **282,** 897–901 (1998).

23. Diguna, L. J., Shen, Q., Kobayashi, J. & Toyoda, T. High efficiency of CdSe quantum-dot-sensitized TiO[sub 2] inverse opal solar cells. *Appl. Phys. Lett.* **91,** 23116 (2007).

24. Kubo, S. *et al.* Tunable photonic band gap crystals based on a liquid crystal-infiltrated inverse opal structure. *J. Am. Chem. Soc.* **126,** 8314–9 (2004).

25. Kim, J.-H. *et al.* Ni-NiO core-shell inverse opal electrodes for supercapacitors. *Chem. Commun. (Camb).* **47,** 5214–5216 (2011).

26. Meng, Y. *et al.* A family of highly ordered mesoporous polymer resin and carbon structures from organic-organic self-assembly. *Chem. Mater.* **18,** 4447–4464 (2006).

27. Jin, J., Nishiyama, N., Egashira, Y. & Ueyama, K. Pore structure and pore size controls of ordered mesoporous carbons prepared from resorcinol/formaldehyde/triblock polymers. *Microporous Mesoporous Mater.* **118,** 218–223 (2009).

28. Meyer, B. Elemental sulfur. *Chem. Rev.* **76,** 367–387 (1976).

29. Robinson, J. P. & Koenig, G. M. Tuning solution chemistry for morphology control of lithium-ion battery precursor particles. *Powder Technol.* **284,** 225–230 (2015).

30. Ren, Y., Shui, H., Peng, C., Liu, H. & Hu, Y. Solubility of elemental sulfur in pure organic solvents and organic solvent-ionic liquid mixtures from 293.15 to 353.15K. *Fluid Phase Equilib.* **312,** 31–36 (2011).

31. Bard, Allen J., Faulkner, L. R. *Electrochemical Methods: Fundamentals and Applications*. (Wiley,

2000).

32. Vogt, H. The Concentration Overpotential of Gas Evolving Electrodes as a Multiple Problem of Mass Transfer. *J. Electrochem. Soc.* **137,** 1179 (1990).

33. Liu, S., Suo, J. & Xiao, J. Effects of surface overpotential at the La1−xSrxCo1−yFeyO3-yttria stabilized zirconia interface in a model solid oxide fuel cell cathode. *Int. J. Hydrogen Energy* **33,** 6322–6326 (2008).

34. Chen, S. R. *et al.* Ordered mesoporous carbon/sulfur nanocomposite of high performances as cathode for lithium-sulfur battery. *Electrochim. Acta* **56,** 9549–9555 (2011).

35. Li, X. *et al.* Optimization of mesoporous carbon structures for lithium–sulfur battery applications. *J. Mater. Chem.* **21,** 16603 (2011).

36. Xu, T. *et al.* Mesoporous Carbon − Carbon Nanotube − Sulfur Composite Microspheres for High-Areal-Capacity Lithium − Sulfur Battery Cathodes. (2013). doi:10.1021/am4035784

37. Shim, J., Striebel, K. A. & Cairns, E. J. The Lithium/Sulfur Rechargeable Cell. *J. Electrochem. Soc.* **149,** A1321 (2002).

38. Xu, R., Li, J. C. M., Lu, J., Amine, K. & Belharouak, I. Demonstration of highly efficient lithium-sulfur batteries. *J. Mater. Chem. A* **3,** 4170–4179 (2015).

39. Xu, R. *et al.* Insight into Sulfur Reactions in Li − S Batteries. *ACS Appl. Mater. Interfaces* (2014).

40. Choi, Y. J., Kim, K. W., Ahn, H. J. & Ahn, J. H. Improvement of cycle property of sulfur electrode for lithium/sulfur battery. *J. Alloys Compd.* **449,** 313–316 (2008).

41. Dysart, A. D. *et al.* Towards Next Generation Lithium-Sulfur Batteries: Non-Conventional Carbon Compartments/Sulfur Electrodes and Multi-Scale Analysis. *J. Electrochem. Soc.* **163,** A730–A741 (2016).

42. Han, S.-C. *et al.* Effect of Multiwalled Carbon Nanotubes on Electrochemical Properties of Lithium/Sulfur Rechargeable Batteries. *J. Electrochem. Soc.* **150,** A889 (2003).

43. Claire, P. Light-Scattering of Coatings Formed from Polystyrene Pigment Particles. **76,** 182–187 (1980).

44. Ramig, A. Opacified latex paint containing plastic polymer particles. 19 (1978).

45. De Jong, W. H. & Borm, P. J. a. Drug delivery and nanoparticles:applications and hazards. *Int. J. Nanomedicine* **3,** 133–149 (2008).

46. Park, S. H. & Xia, Y. Assembly of Mesoscale Particles over Large Areas and Its Application in Fabricating Tunable Optical Filters. *Langmuir* **15,** 266–273 (1999).

47. Liu, B., Wang, Y., Zhang, M. & Zhang, H. Initiator systems effect on particle coagulation and particle size distribution in one-step emulsion polymerization of styrene. *Polymers (Basel).* **8,** 1–14 (2016).

48. Yamamoto, T., Kanda, Y. & Higashitani, K. Nucleation and growth process of polystyrene particle investigated by AFM. *J. Chem. Eng. Japan* **39,** 596–603 (2006).

49. Tuin, G., Peters, A. C. I., van Diemen, A. J. G. & Stein, H. N. Preparation of Large Monodisperse Polystyrene Particles by a One Step Surfactant-Free Emulsion Polymerization. *Journal of Colloid and Interface Science* **158,** 508–510 (1993).

50. Ho, C. C., Keller, A., Odell, J. A. & Ottewill, R. H. Preparation of monodisperse ellipsoidal polystyrene particles. *Colloid & Polymer Science* **271,** 469–479 (1993).

51. Gong, T. & Wang, C. C. Preparation of highly cross-linked monodispersed functional polystyrene particles by utilizing the delayed addition method. *J. Mater. Sci.* **43,** 1926–1932 (2008).

52. Wang, H. *et al.* Journals Graphene-Wrapped Sulfur Particles as a Rechargeable Lithium – Sulfur

Battery Cathode Material ... Graphene-Wrapped Sulfur Particles as a Rechargeable Lithium – Sulfur Battery Cathode Material with High Capacity and Cycling Stability. *History* 1–4 (2011). doi:10.1021/nl200658a

53. Yin, L., Wang, J., Lin, F., Yang, J. & Nuli, Y. Polyacrylonitrile/graphene composite as a precursor to a sulfur-based cathode material for high-rate rechargeable Li–S batteries. *Energy Environ. Sci.* **5,** 6966 (2012).

54. Li, H. *et al.* Dense integration of graphene and sulfur through the soft approach for compact lithium/sulfur battery cathode. *Nano Energy* **12,** 468–475 (2015).

55. Pu, X., Yang, G. & Yu, C. Liquid-type cathode enabled by 3D sponge-like carbon nanotubes for high energy density and long cycling life of Li-S Batteries. *Adv. Mater.* **26,** 7456–7461 (2014).

56. Tang, C. *et al.* Nitrogen-doped aligned carbon nanotube/graphene sandwiches: Facile catalytic growth on bifunctional natural catalysts and their applications as scaffolds for high-rate lithium-sulfur batteries. *Adv. Mater.* **26,** 6100–6105 (2014).

57. Sun, L. *et al.* Sulfur Embedded in a Mesoporous Carbon Nanotube Network as a Binder-Free Electrode for High-Performance Lithium–Sulfur Batteries. *ACS Nano* acsnano.5b06675 (2015). doi:10.1021/acsnano.5b06675

58. Agostini, M. *et al.* A lithium-ion sulfur battery based on a carbon-coated lithium-sulfide cathode and an electrodeposited silicon-based anode. *ACS Appl. Mater. Interfaces* **6,** 10924–10928 (2014).

59. Liang, Z. *et al.* Sulfur cathodes with hydrogen reduced titanium dioxide inverse opal structure. *ACS Nano* **8,** 5249–5256 (2014).

60. Ferrari, a. & Robertson, J. Interpretation of Raman spectra of disordered and amorphous carbon. *Phys. Rev. B* **61,** 14095–14107 (2000).

61. Yeon, J.-T. *et al.* Raman Spectroscopic and X-ray Diffraction Studies of Sulfur Composite

Electrodes during Discharge and Charge. *J. Electrochem. Soc.* **159,** A1308–A1314 (2012).